Supplement of The Cryosphere, 18, 3787–3805, 2024
https://doi.org/10.5194/tc-18-3787-2024-supplement

The Cryosphere Open Access EGU

Supplement of

Microstructure-based modelling of snow mechanics: experimental evaluation of the cone penetration test

Clémence Herny et al.

Correspondence to: Clémence Herny (clemence.herny@gmail.com)

S1 Numerical sensitivity analysis

Before performing DEM simulations on complete numerical samples, a series of numerical sensitivity analyses have been conducted to understand the dependencies of the model results on numerical parameters and choose optimised values. To limit the time allocated to this work, these sensitivity analyses have been performed on a reduced numerical sample, except for the analysis on numerical sample size. We chose a cubic numerical sample with a side length of 8 mm and a rod radius 6 times smaller than the actual one. The detailed results of these sensitivity analyses are presented in the following subsections.

S1.1 Sensitivity to grain shape representation

In the DEM simulations, a snow grain is modelled by a clump of spheres capturing its arbitrary shape. The downside of this approach is the potentially large number of spheres and interactions, resulting in time-consuming computation. To run DEM simulations on centimetre-sized numerical samples, involving thousands of grains, the grain shape representation had to be optimised to preserve a reliable mechanical behaviour along with a reasonable computing time. The two parameters used in the grain shape representation, (1) the minimum sphere radius L and (2) the minimum sphere coverage S, have been varied. Their influence on the sphere number (and thus on the computation time), the grain number, the interaction number, the volumetric representation and the mechanical response were investigated to establish the optimal choice of parameters.

This sensitivity analysis has been repeated for the four snow samples studied, i.e. RG, RGlr, DH and PP. Indeed, each snow type presents different grain characteristics and the optimised grain shape representation parameters may differ among them.

The geometrical accuracy of the grain shape representation is evaluated through the volumetric error E_V. This quantity is computed as the ice volume difference between the original and the approximated image of the grains, divided by the ice volume of the original grain image (hence $E_V = 0$ corresponds to perfectly reconstructed grains). The medial axis method used for the grain approximation implies an underestimation of the grain volume (Coeurjolly and Montanvert, 2017, Mede et al., 2018) and the smallest grains might not be represented. The global trend is that E_V decreases with the number of spheres increasing (Table S1 and Fig. S1). We also observe that E_V increases with L and S.

To evaluate the mechanical accuracy of the DEM simulations, a mechanical error E_M is computed similarly as in Mede et al., 2018. This quantity is defined as the normalised root mean square error of the force profile relative to a reference simulation (Table S1 and Fig. S1). The reference simulation is defined as the $L - S$ combination values providing the lowest value of E_V. Note that E_M is computed on force profiles averaged over a rolling window Δz = 3 mm to smooth out the fluctuations. The general trend observed is an increase of E_M with E_V. However, we notice that relatively low E_M and low E_V values can be reached for a moderate number of spheres (Table S1 and Fig. S1).

Sample	L (vx)	S	Number of spheres	Number of grains	Number of initial cohesive interactions between grains	E_V (%)	E_M (%)
RG	2	0.2	695380	8362	14839	10.5	0.0

	2	0.3	478330	8362	14839	14.6	11.7
	2	0.5	298981	8362	14839	22.6	34.6
	2	0.8	199996	8362	14839	35.2	55.1
	3	0.2	487094	8186	14642	14.2	21.6
	3	0.3	340295	8186	14642	17.7	45.3
	3	0.5	212439	8186	14642	24.9	62.4
	5	0.2	153208	6156	10501	41.1	5.0
	5	**0.3**	**112139**	**6156**	**10501**	**42.9**	**5.3**
	5	0.5	74243	6156	10501	46.6	20.3
RGlr	3	0.2	148078	2065	5111	9.2	0.0
	3	0.3	105859	2065	5111	13.1	21.9
	3	0.5	69365	2065	5111	21.3	6.0
	5	0.2	89053	1964	4963	11.1	4.8
	5	**0.3**	**61251**	**1964**	**4963**	**14.9**	**4.2**
	5	0.5	38256	1964	4963	22.5	24.3
	8	0.2	47924	1695	4363	18.2	44.6
DH	2	0.2	519856	3109	6144	8.0	0.0
	2	0.3	360490	3109	6144	11.6	6.2
	2	0.5	227247	3109	6144	19.5	32.3
	2	0.8	154331	3109	6144	32.9	15.9
	3	0.2	386882	3056	6085	10.2	5.9
	3	0.3	271824	3056	6085	13.6	22.0
	3	0.5	172874	3056	6085	20.8	32.2
	5	**0.2**	**162919**	**2527**	**5147**	**24.9**	**14.3**
	5	0.3	116547	2527	5147	27.4	25.8
	5	0.5	76067	2527	5147	32.6	13.0
PP	2	0.1	851438	19832	26217	17.4	0.0
	2	0.2	590590	19832	26217	20.3	1.7
	2	0.3	448132	19832	26217	24.4	2.9
	2	**0.5**	**306191**	**19832**	**26217**	**32.0**	**10.3**
	2	0.8	207615	19828	26212	44.0	24.4

Table S1 : Summary of the sensitivity analysis to the grain shape representation parameters: number of spheres, number of grains, number of cohesive interactions, volumetric error E_V and mechanical error E_M for each parameter combination. Note that E_M = 0 for the chosen reference simulation. The selected numerical parameters of each snow sample and their respective characteristics are highlighted with bold text.

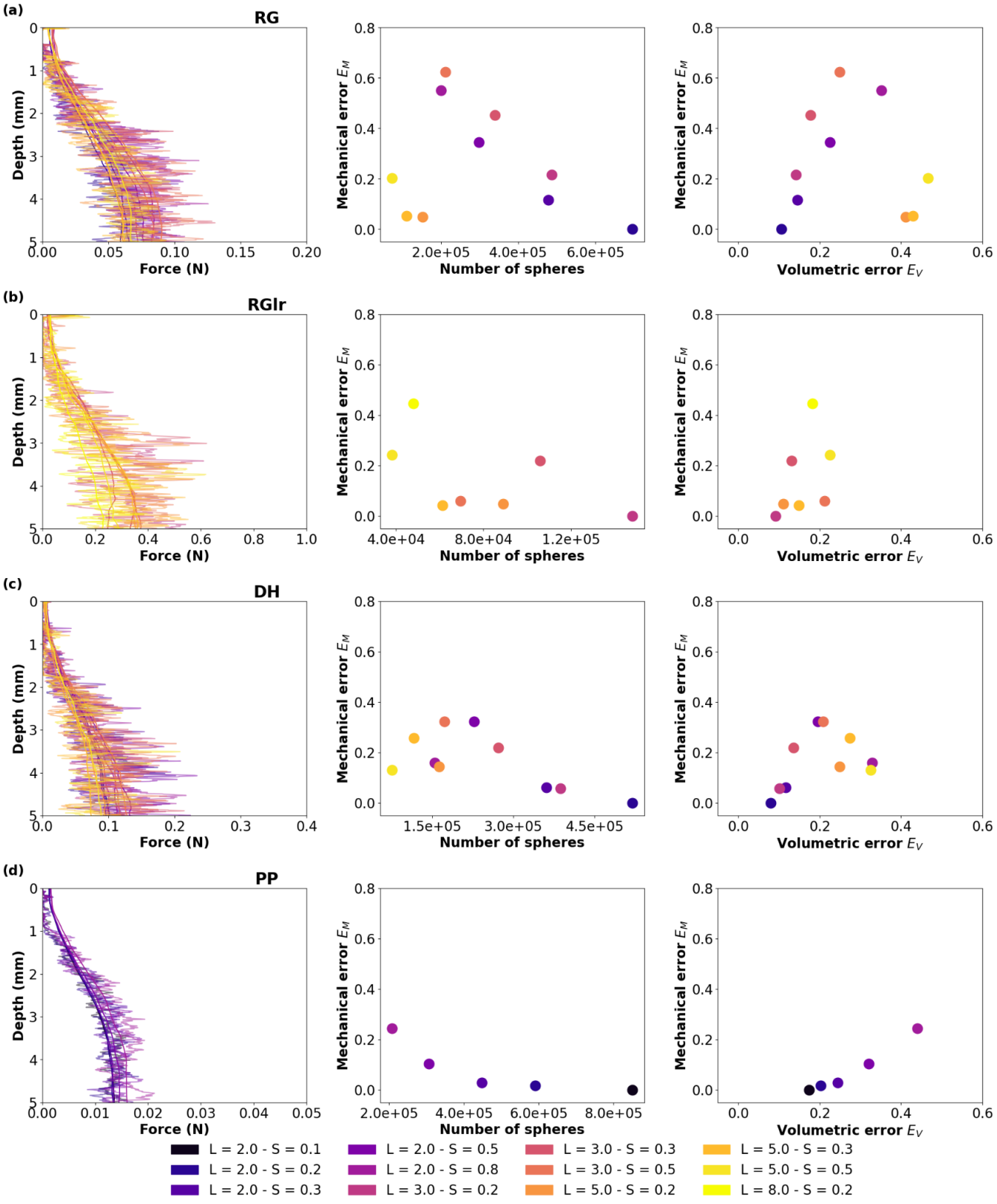
(a)
RG
(b)
RGlr
(c)
DH
(d)
PP
Depth (mm)
Force (N)
Mechanical error E_M
Number of spheres
Volumetric error E_V
L = 2.0 - S = 0.1
L = 2.0 - S = 0.2
L = 2.0 - S = 0.3
L = 2.0 - S = 0.5
L = 2.0 - S = 0.8
L = 3.0 - S = 0.2
L = 3.0 - S = 0.3
L = 3.0 - S = 0.5
L = 5.0 - S = 0.2
L = 5.0 - S = 0.3
L = 5.0 - S = 0.5
L = 8.0 - S = 0.2

Figure S1: Results of the sensitivity analysis to grain shape representation parameters *L* and *S* for the samples RG, RGlr, DH and PP. (a) Full force profiles (light colour lines) and smoothed profiles (force averaged over a rolling window of 3 mm). (b) Evolution of the volumetric error E_V with respect to the number of spheres for each *L* – *S* combination. (c) Evolution of volumetric error E_V vs mechanical error E_M. For each sample, the reference run to compute E_M corresponds to the numerical sample with the maximum of spheres.

In order to choose the shape parameters for each snow type, we selected the combination allowing to have E_M below a threshold of 20% with the lowest number of spheres. For some samples (notably RG), this choice implies selecting a numerical sample with a relatively high value of E_V.

S1.2 Sensitivity to numerical sample size

A larger numerical sample size implies larger numbers of grains, spheres and interactions, which directly affects the computation time. The CPT configuration leaves scope for adapting the size of the numerical sample without introducing border effects. To evaluate the influence of this parameter, we calculated the mechanical error E_M (Sect. S1.1) between the force profiles obtained for different numerical sample sizes relative to a reference simulation computed with the largest possible sample size along the x and y axis (14.1 mm side length). For all these simulations, the tip radius is set to 2.5 mm, consistent with that of the SMP (Sect. 2.1.3) and the depth of the numerical sample is set at a constant value of 12 mm. This analysis was performed only for the sample RGlr. Since this sample is characterised by the largest grain size (Table 1), it is the most likely to be affected by border effects. We assume that the results can be applied to the other snow samples with smaller grain sizes.

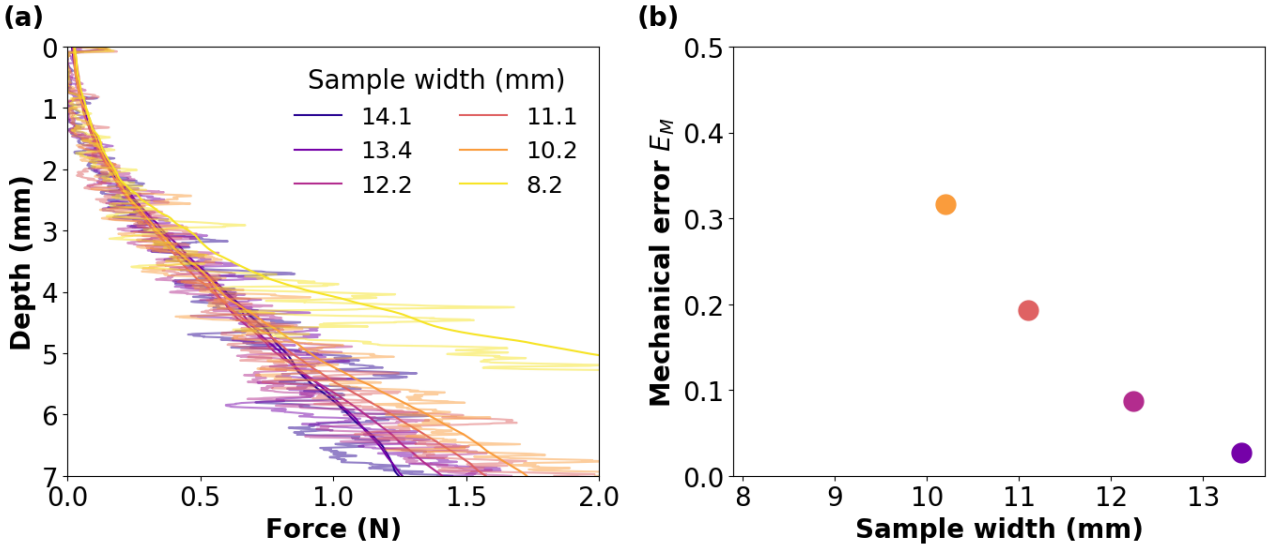

Figure S2: Results of the sensitivity analysis on the numerical sample size. (a) Full force profiles (light colour lines) and smoothed profiles (force averaged over a rolling window of 3 mm). (b) Mechanical error E_M as a function of the numerical sample width. The reference force profile corresponds to a width of 14.1 mm. The data point corresponding to a sample width of 8.2 mm is out of the range of the plot. The results were obtained for the RGlr sample.

As shown in Fig. S2, it was observed that the numerical sample size can be reduced to 12 mm while still keeping a mechanical error E_M of less than 20% and a force profile well consistent with that of the reference case. Below this limit of 12 mm, typically, border effects become significant. Based on these results, our simulations were performed with a sample side length of 12.4 mm.

S1.3 Sensitivity to motion equation parameters

To reduce the computation time, the numerical time step can be increased by artificially increasing the mass of the grains through the definition of a mass factor f (Eq. (6), Sect. 2.2.3). The results of a dedicated sensitivity analysis show that mass factors up to 1 x 10^4 provide consistent results with those obtained with $f = 1$ (Fig. S3). All the simulation results presented in the paper were obtained with a mass factor $f = 1 \times 10^2$.

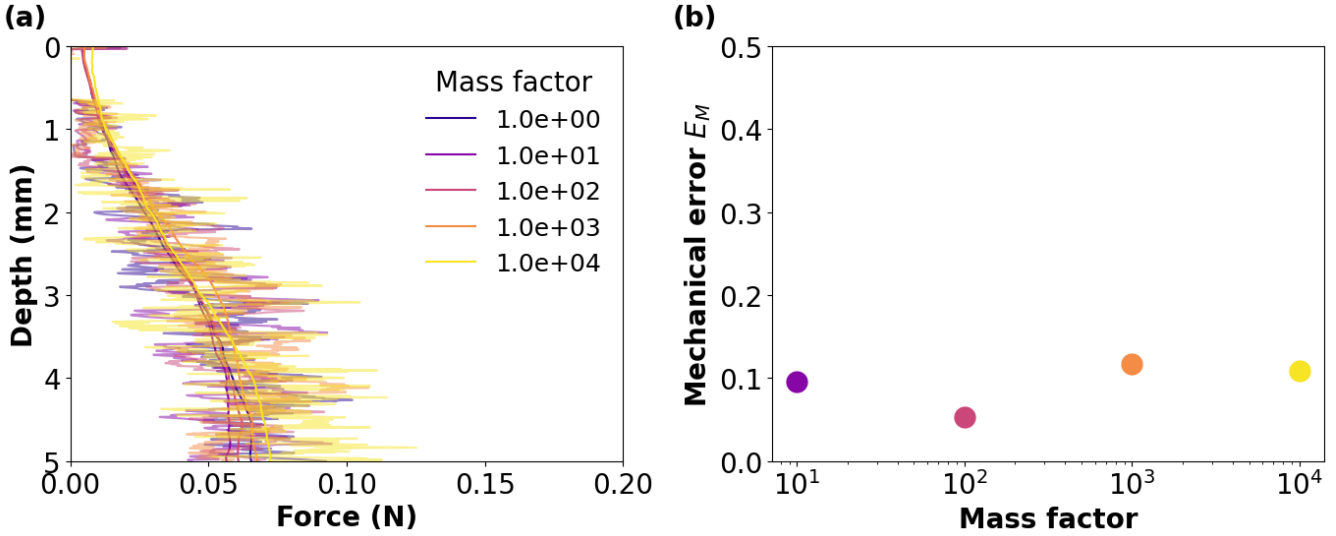

Figure S3: Results of the sensitivity analysis to the mass factor. (a) Full force profiles (light colour lines) and smoothed profiles (force averaged over a rolling window of 3 mm). (b) Mechanical error E_M as a function of the mass factor. The reference profile corresponds to a mass factor of 1. The results were obtained for the RG sample.

The Cundall's non-viscous damping coefficient Λ is applied to prevent numerical oscillations. The sensitivity analysis of this parameter (Fig. S4) shows that it does not have a strong influence on the resulting force profiles. A value of 0.05 was chosen for our simulations.

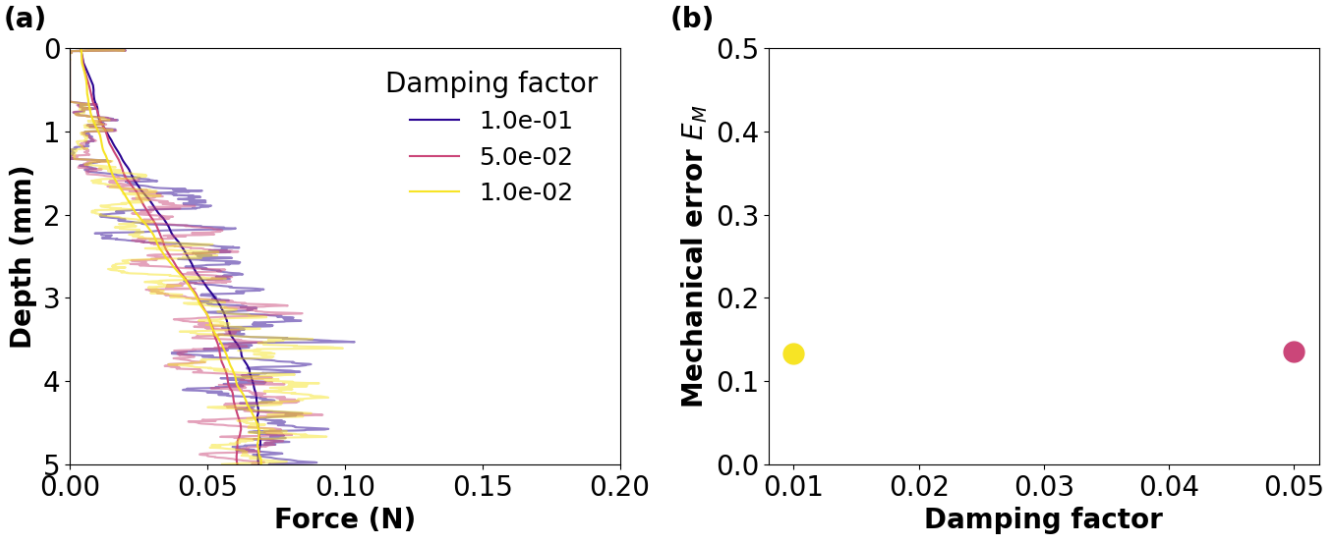

Figure S4: Results of the sensitivity analysis to the Cundall's non-viscous damping coefficient. (a) Full force profiles (light-colour lines) and smoothed profiles (force averaged over a rolling window of 3 mm). (b) Mechanical error E_M as a function of the damping factor. The reference force profile corresponds to a damping factor of 0.1. The results were obtained for the RG sample.

S1.4 Rigid grain assumption

To be consistent with the DEM approach, the overlap between spheres in contact must remain under a few percent of the sphere's radius (rigid grain assumption). Since Young's modulus, and thus contact stiffness (Sect. 2.2.2), was varied in our study, we verified that the rigid grain assumption remained valid for all the values tested. Figure S5 shows that for Young's modulus values in the range chosen for our study (E = 1 x 10^8-1 x 10^{10} Pa), the relative sphere overlap effectively remains negligible (under 1%). For lower values of Young's modulus ($E \leq 1 \times 10^7$ Pa), relative overlap increases up to several percent, which violates the rigid grain assumption.

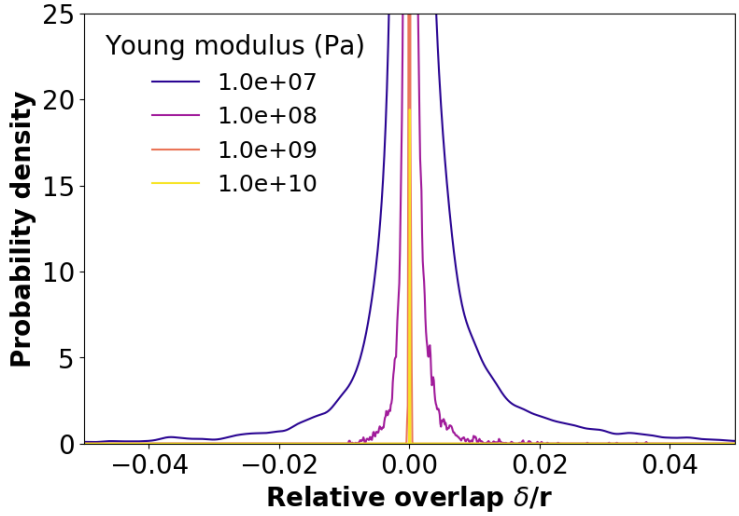

Figure S5: Distribution of relative grain overlaps for a penetrating depth of 3 mm and for different values of Young's modulus *E* (Pa). The results were obtained for the RG sample.

S2 Additional results

S2.1 Simulated Cone Penetration Tests

S2.1.1 RGlr sample

The macroscopic force profile displays an 'S' shape with a first transition at around 2.5 mm depth, and a second transition at around 8 mm depth (Fig. S6 (a)).

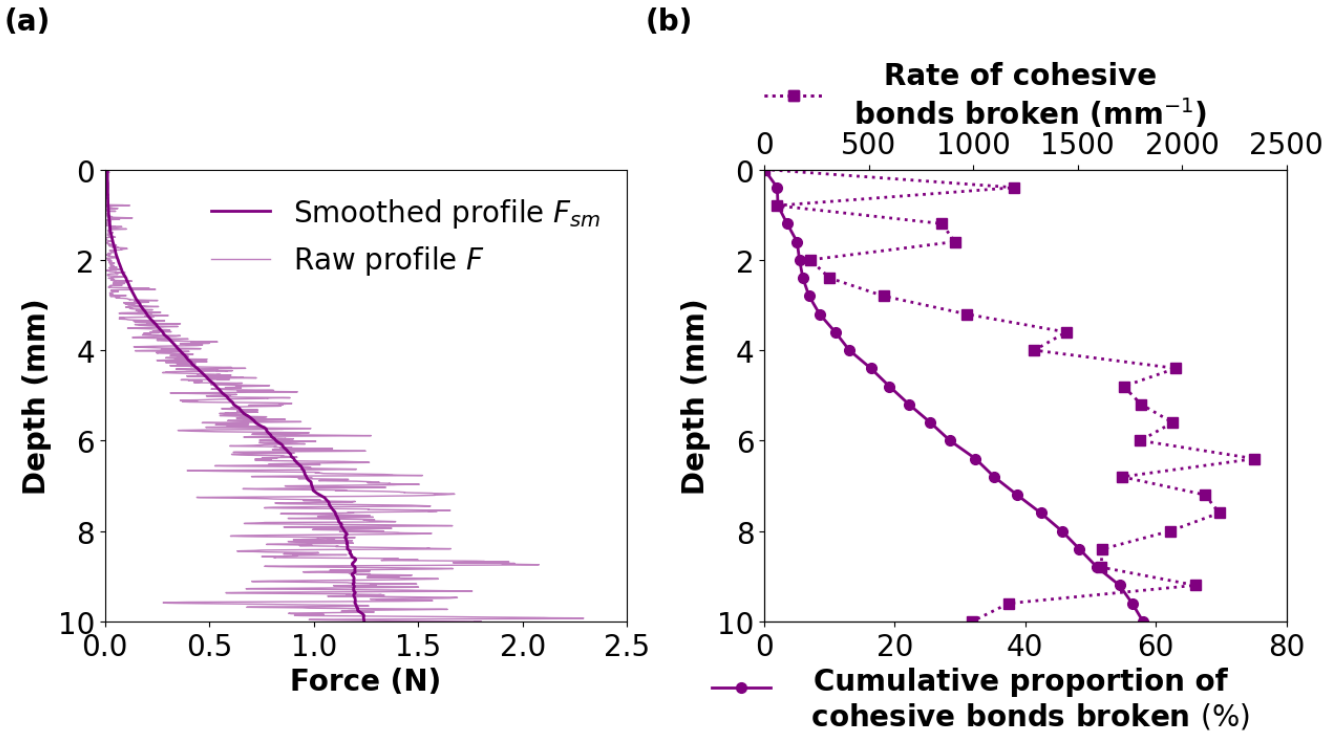

Figure S6: (a) Force *F* as a function of penetration depth (light line) obtained for the RGlr sample. The superposed smoothed profile (bold line) F_{sm} corresponds to the average force value over a rolling window of 3 mm. (b) Rate of cohesive bonds broken by mm and cumulative proportion of cohesive bonds broken (%) as a function of tip penetration depth. The initial number of cohesive bonds is indicated in Table 1. Results are obtained with the mechanical parameters indicated in Table 3.

About 60% of the initial cohesive interactions broke over 10 mm of penetration, corresponding to an average rate of ~1400 broken bonds mm^{-1} (Fig. S6 (b)).

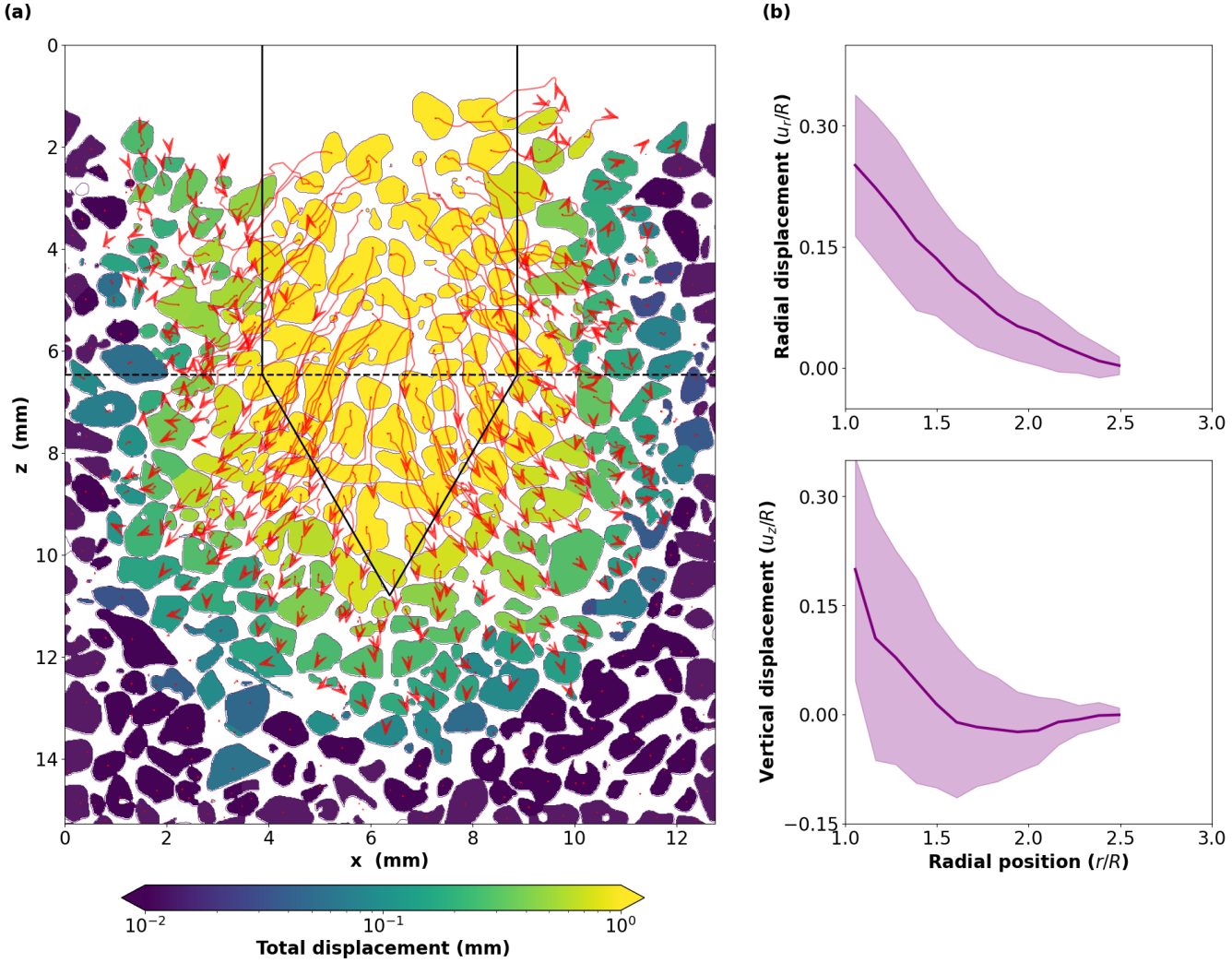

Figure S7: (a) (a) Simulated grain displacement map for the RGlr sample. The red arrows indicate the grain trajectories while the tip is penetrating (sampling = 0.4 mm). White grains correspond to grains that are not represented in the DEM simulation. The final tip position is indicated by the black solid lines. The horizontal black dashed line indicates the cone top. (b) Radial (upper panel) and vertical (lower panel) displacement profiles (red curves) for the RG sample. These profiles represent averages computed from the sample surface to the cone top. By convention, downward (respectively upward) movement corresponds to positive (respectively negative) values of vertical displacement. The shadowed areas around the solid lines represent the standard deviation of grain displacements. The results are obtained with the mechanical parameters indicated in Table 3.

For the RGlr sample, the displacement field presents complex characteristics (Fig. S7 (a)). Close to the surface of the sample, the grain trajectories are oriented upward. Predominantly downward displacements are then observed for larger depths, below the cone top.

The observed curved trajectory, oriented upward in the area located between the sample surface and the cone top, is transcribed in the average vertical displacement profile (Fig. S7 (b)) which essentially shows upward movement and reaches zero at a

radial position around 2.4*R*. Recall that this average profile is computed from the sample surface to the cone top. The radial displacement profile follows a quasi-linear trend, reaching 0 at a radial position around 2.5*R*.

S2.1.2 DH sample

The macroscopic force profile shows a first transition at around 2 mm depth (Fig. S8 (a)). At a depth of about 8 mm, the smoothed averaged force profile seems to stabilise at a nearly constant value, but this is less obvious than for the other samples.

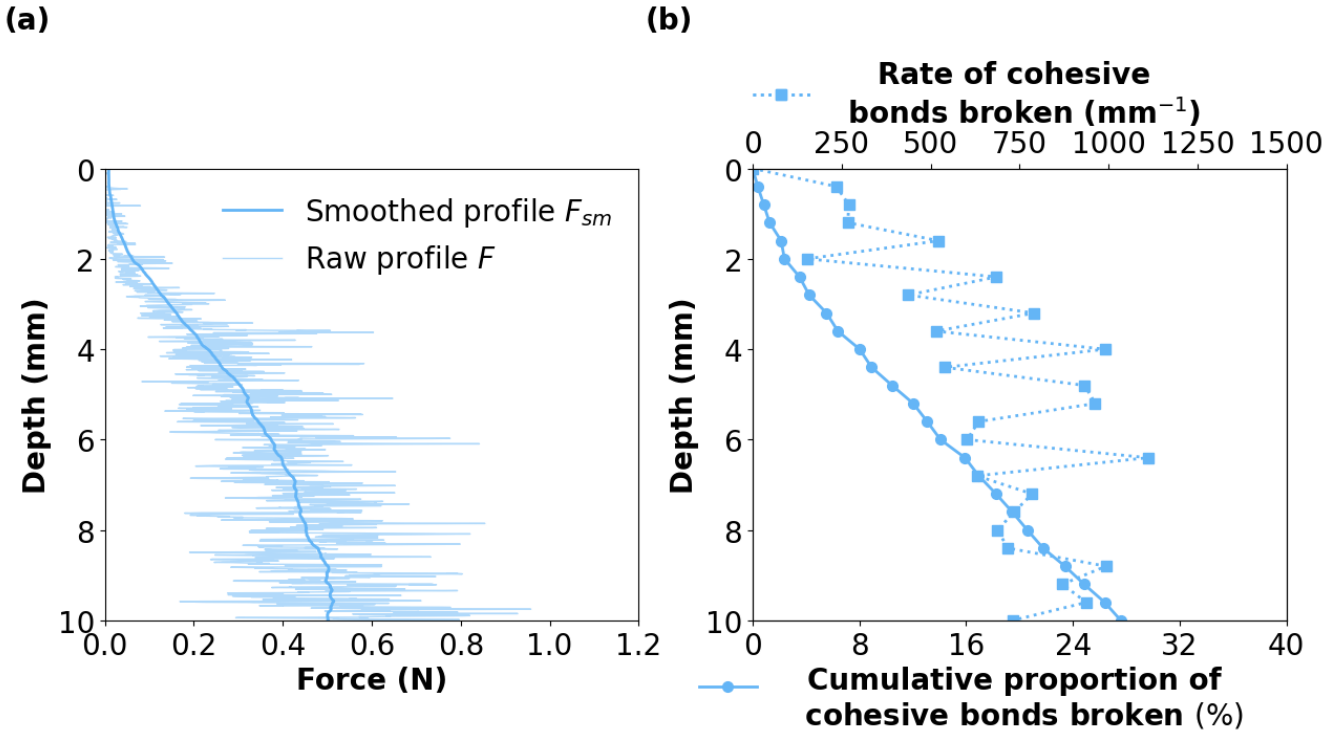

Figure S8: (a) Force *F* as a function of penetration depth (light line) obtained for the DH sample. The superposed smoothed profile (bold line) F_{sm} corresponds to the average force value over a rolling window of 3 mm. (b) Rate of cohesive bonds broken by mm and cumulative proportion of cohesive bonds broken (%) as a function of tip penetration depth. The initial number of cohesive bonds is indicated in Table 1. Results are obtained with the mechanical parameters indicated in Table 3.

About 28% of the cohesive interactions broke over 10 mm of penetration, corresponding to an average rate of ~650 bond failures mm^{-1} (Fig. S8 (b)). Unlike the other samples, no clear slope change is observed in the cumulative profile at a depth corresponding to the first transition in the force profile. The rate of bond failures shows a quasi-constant value over the entire depth of the profile.

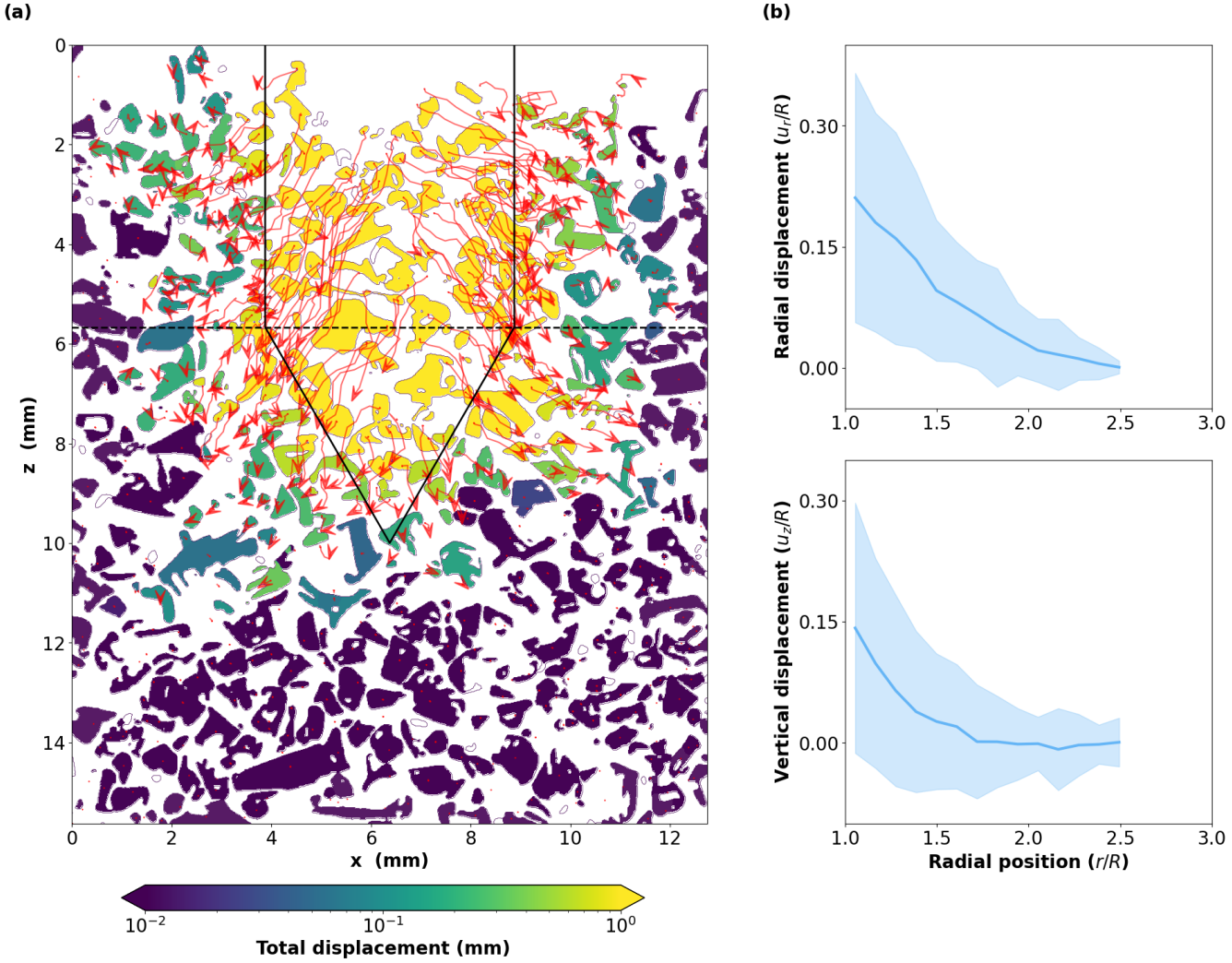

Figure S9: (a) Simulated grain displacement map for the DH sample. The red arrows indicate the grain trajectories while the tip is penetrating (sampling = 0.4 mm). White grains correspond to grains that are not represented in the DEM simulation. The final tip position is indicated by the black solid lines. The horizontal black dashed line indicates the cone top. (b) Radial (upper panel) and vertical (lower panel) displacement profiles (red curves) for the RG sample. These profiles represent averages computed from the sample surface to the cone top. By convention, downward (respectively upward) movement corresponds to positive (respectively negative) values of vertical displacement. The shadowed areas around the solid lines represent the standard deviation of grain displacements. The results are obtained with the mechanical parameters indicated in Table 3.

Grain trajectories for the DH sample show globally a similar pattern as that observed for the RG sample (F. S9 (a)). Both radial and vertical displacement profiles display a pronounced decreasing trend, and reach zero at radial positions of about 2.4R and 2.0R, respectively (Fig. S9 (b)). The vertical profile indicates a dominant downward movement of the grains close to the tip.

S2.1.3 PP sample

The macroscopic force profile displays an 'S' shape with a first transition at around 2.0 mm depth, and a second transition at around 6 mm depth (Fig. S10 (a)). Compared to the other samples, the second transition and the stabilisation of the force to a quasi-constant level occurs at a shallower penetration depth.

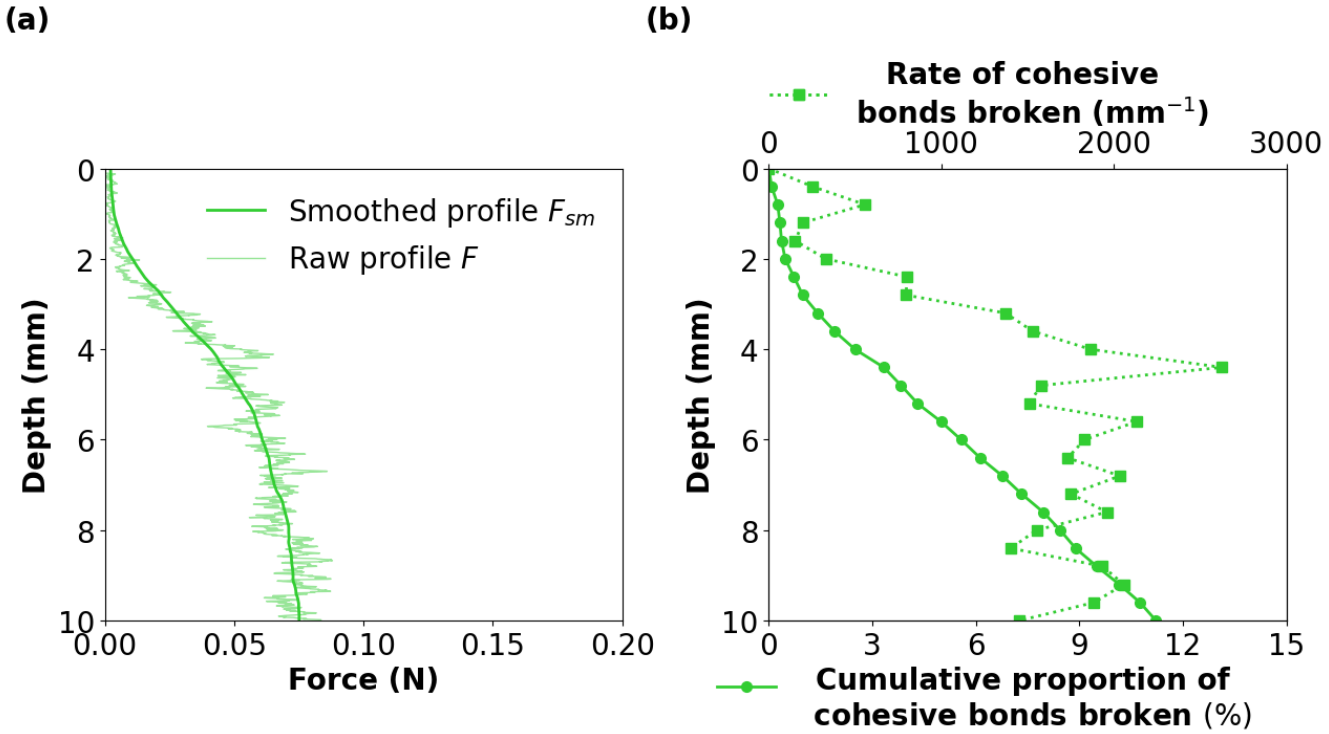

Figure S10: (a) Force *F* as a function of penetration depth (light line) obtained for the PP sample. The superposed smoothed profile (bold line) F_{sm} corresponds to the average force value over a rolling window of 3 mm. (b) Rate of cohesive bonds broken by mm and cumulative proportion of cohesive bonds broken (%) as a function of tip penetration depth. The initial number of cohesive bonds is indicated in Table 1. Results are obtained with the mechanical parameters indicated in Table 3.

About 12% of the cohesive interactions broke over 10 mm of penetration, corresponding to an average rate of ~1360 bond failures mm^{-1} (Fig. S10 (b)).

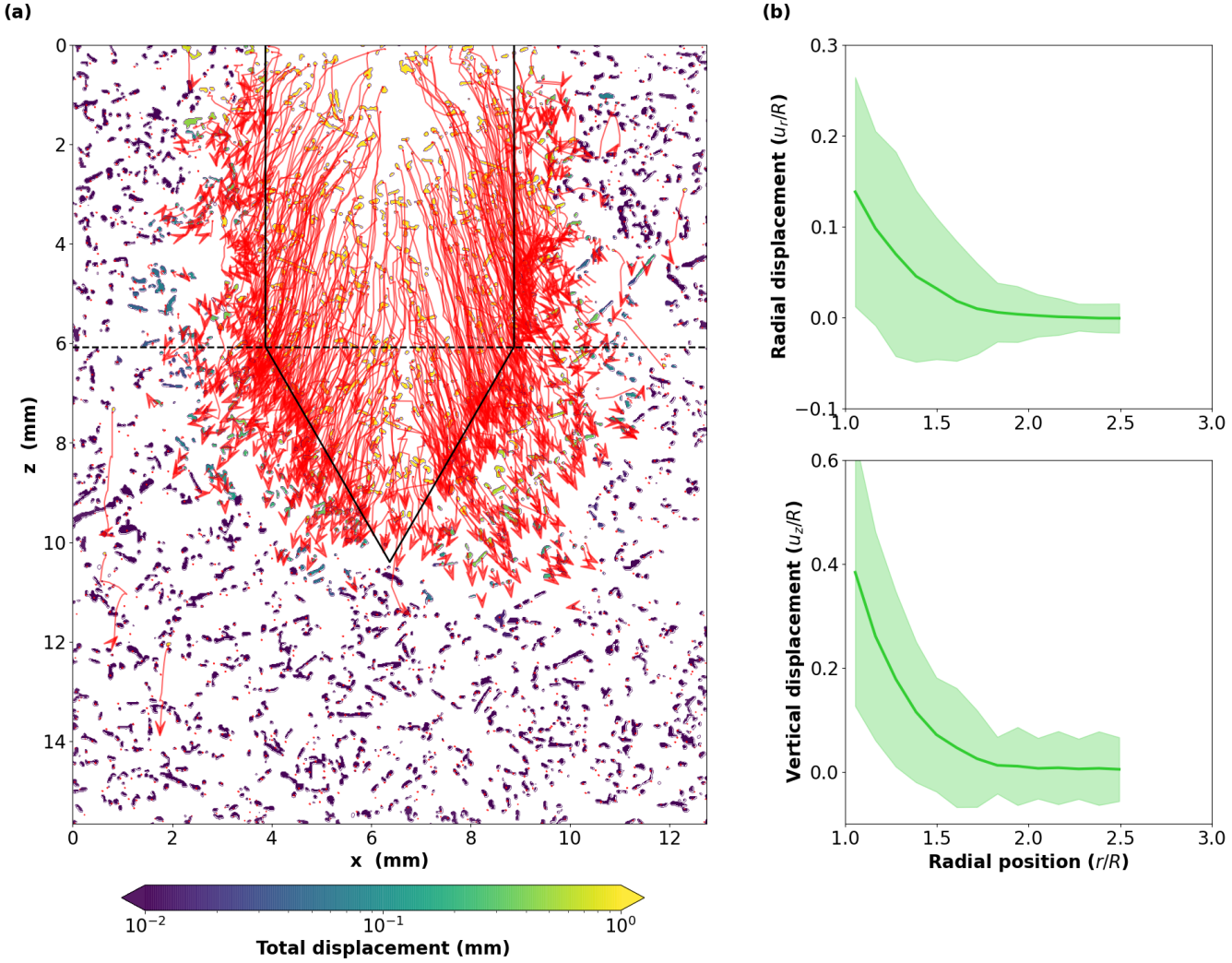

Figure S11: (a) Simulated grain displacement map for the PP sample. The red arrows indicate the grain trajectories while the tip is penetrating (sampling = 0.4 mm). White grains correspond to grains that are not represented in the DEM simulation. The final tip position is indicated by the black solid lines. The horizontal black dashed line indicates the cone top. (b) Radial (upper panel) and vertical (lower panel) displacement profiles (red curves) for the RG sample. These profiles represent averages computed from the sample surface to the cone top. By convention, downward (respectively upward) movement corresponds to positive (respectively negative) values of vertical displacement. The shadowed areas around the solid lines represent the standard deviation of grain displacements. The results are obtained with the mechanical parameters indicated in Table 3.

Figure S11a shows the total displacement of the grains and their respective trajectories for the PP sample. The largest displacements (up to several mm) are observed for grains initially located on the trajectory of the tip, while around the tip the displacements are < 1 mm and are mainly localised close to the tip. Grain trajectories indicate that grains are pushed downward from each side of the tip. The grains initially located in the middle of the tip path display a quasi-straight vertical trajectory. The trajectories become more radial away from the tip medial axis, with the grains being also pushed aside. The grain

trajectories are predominantly linear, with a rather vertical orientation at the cone top and a more radial orientation near the tip. Both radial and vertical displacement profiles display a pronounced decreasing trend, and reach zero at radial positions of about 1.7*R* and 2.0*R*, respectively (Fig. S11 (b)). The vertical profile attests to a dominant downward movement of the grains close to the tip.

S2.2 Mechanical parameters sensitivity analysis

In this section, the figures obtained for the mechanical parameters sensitivity analysis are presented respectively for each sample. The description and interpretation of the plots can be found in the core of the article (Sect. 3.2 and 3.3).

S2.2.1 RG sample

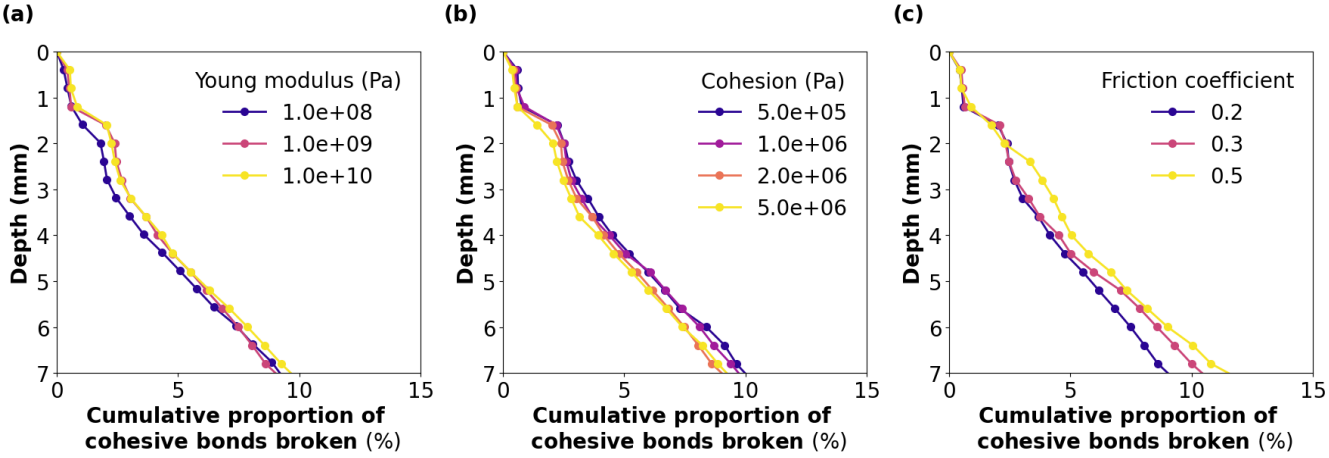

Figure S12: Influence of mechanical parameters on the cumulative number of cohesive bonds as a function of tip penetration depth obtained with DEM numerical simulations of CPT. The sensitivity analysis has been performed on (a) Young's modulus *E* (Pa) (*C* = 2.0 x 10^6 Pa and *tan(φ)* = 0.2), (b) the Cohesion *C* (Pa) (*E* = 1.0 x 10^9 Pa and *tan(φ)* = 0.2) and (c) the Friction coefficient *tan(φ)* (*E* = 1.0 x 10^9 Pa and *C* = 2.0 x 10^6 Pa).

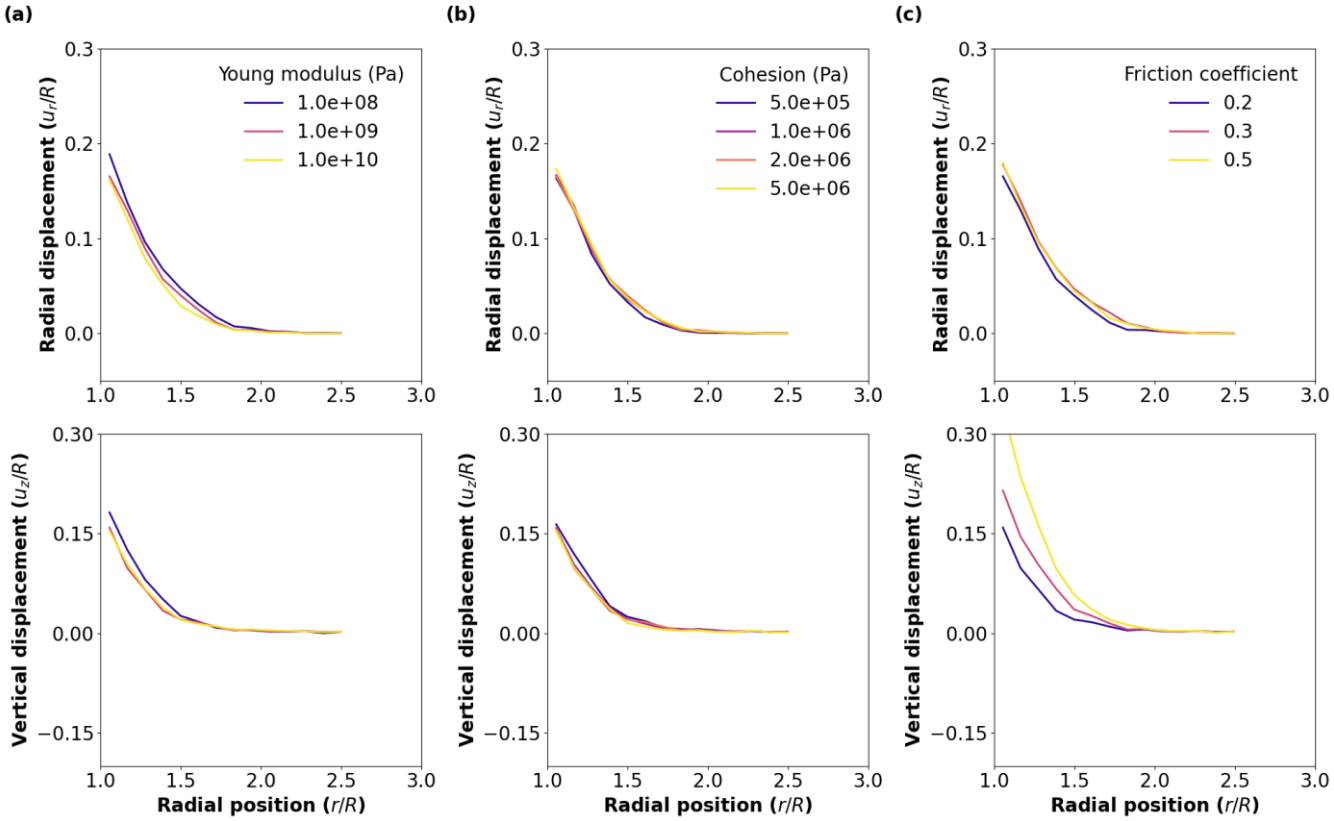

Figure S13: Influence of mechanical parameters on the radial (top) and vertical (bottom) displacement profile obtained with DEM numerical simulations of CPT. The sensitivity analysis has been performed on (a) Young's modulus *E* (Pa) (*C* = 2.0 x 10^6 Pa and *tan(φ)* = 0.2), (b) the Cohesion *C* (Pa) (*E* = 1.0 x 10^9 Pa and *tan(φ)* = 0.2) and (c) the Friction coefficient tan(φ) (*E* = 1.0 x 10^9 Pa and *C* = 2.0 x 10^6 Pa).

S2.2.2 RGlr sample

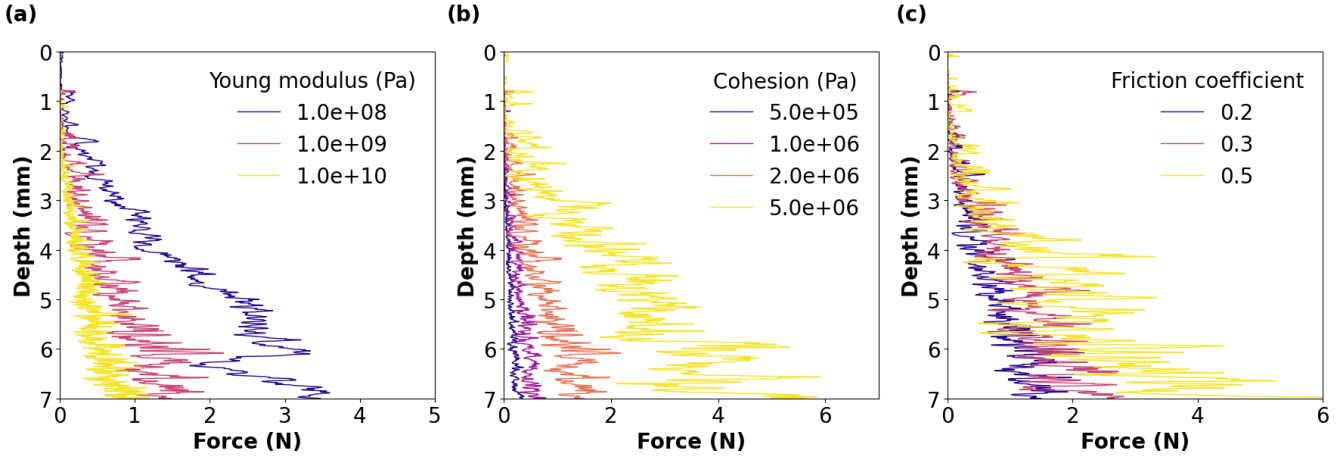

**Figure S14*:* Influence of mechanical parameters on the force profile obtained with DEM numerical simulations of CPT. The sensitivity analysis has been performed on (a) Young's modulus *E* (Pa) (*C* = 2.0 x 10^6 Pa and *tan(φ)* = 0.2), (b) the Cohesion *C* (Pa) (*E* = 1.0 x 10^9 Pa and *tan(φ)* = 0.2) and (c) the Friction coefficient *tan(φ)* (*E* = 1.0 x 10^9 Pa and *C* = 2.0 x 10^6 Pa).

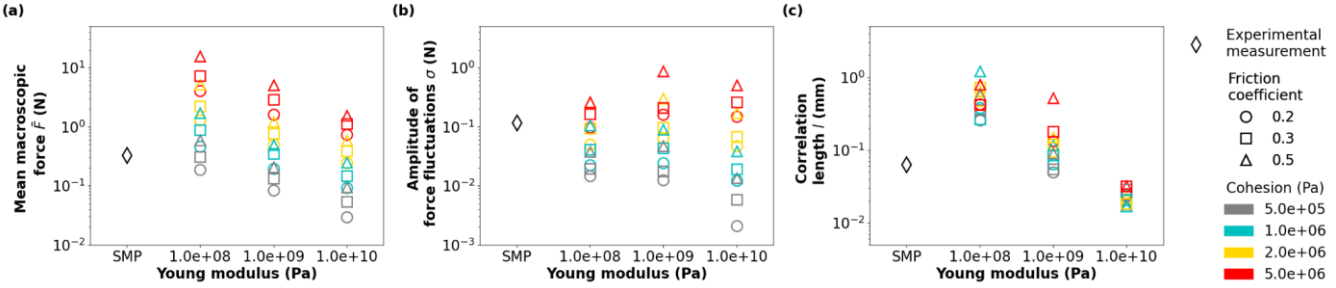

Figure S15*:* Evolution of statistical indicators as a function of Young's modulus, cohesion and friction angle: (a) Mean macroscopic force $\bar{F}$, (b) amplitude of force fluctuations σ, and (c) correlation length *l*. The experimental results (black diamonds) have been added to the plots. The results presented here correspond to the RGlr sample.

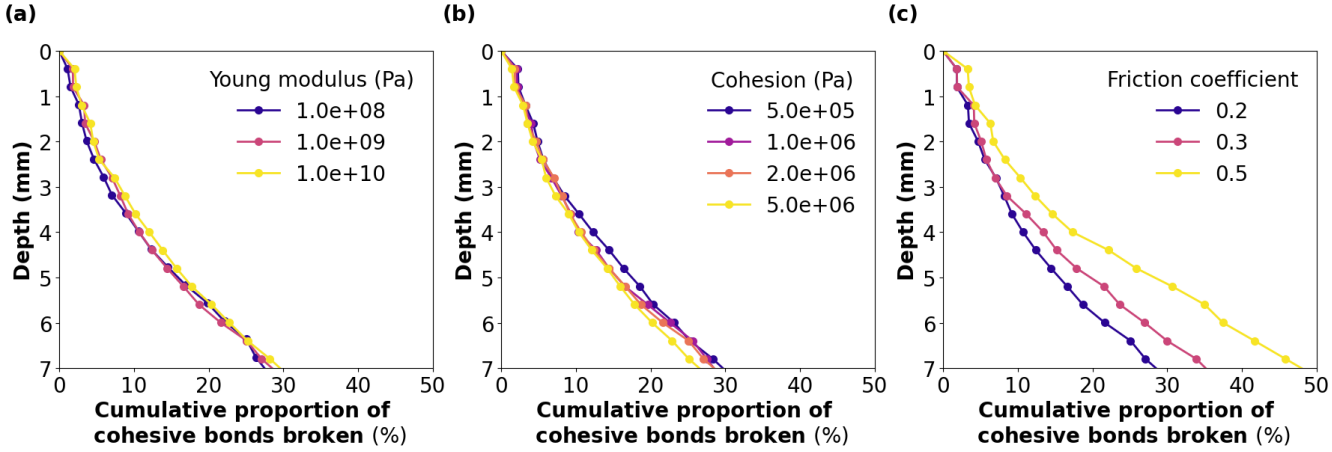

Figure S16: Influence of mechanical parameters on the cumulative number of cohesive bonds as a function of tip penetration depth obtained with DEM numerical simulations of CPT. The sensitivity analysis has been performed on (a) Young's modulus *E* (Pa) (*C* = 2.0 x 10^6 Pa and *tan(φ)* = 0.2), (b) the Cohesion *C* (Pa) (*E* = 1.0 x 10^9 Pa and *tan(φ)* = 0.2) and (c) the Friction coefficient *tan(φ)* (*E* = 1.0 x 10^9 Pa and *C* = 2.0 x 10^6 Pa).

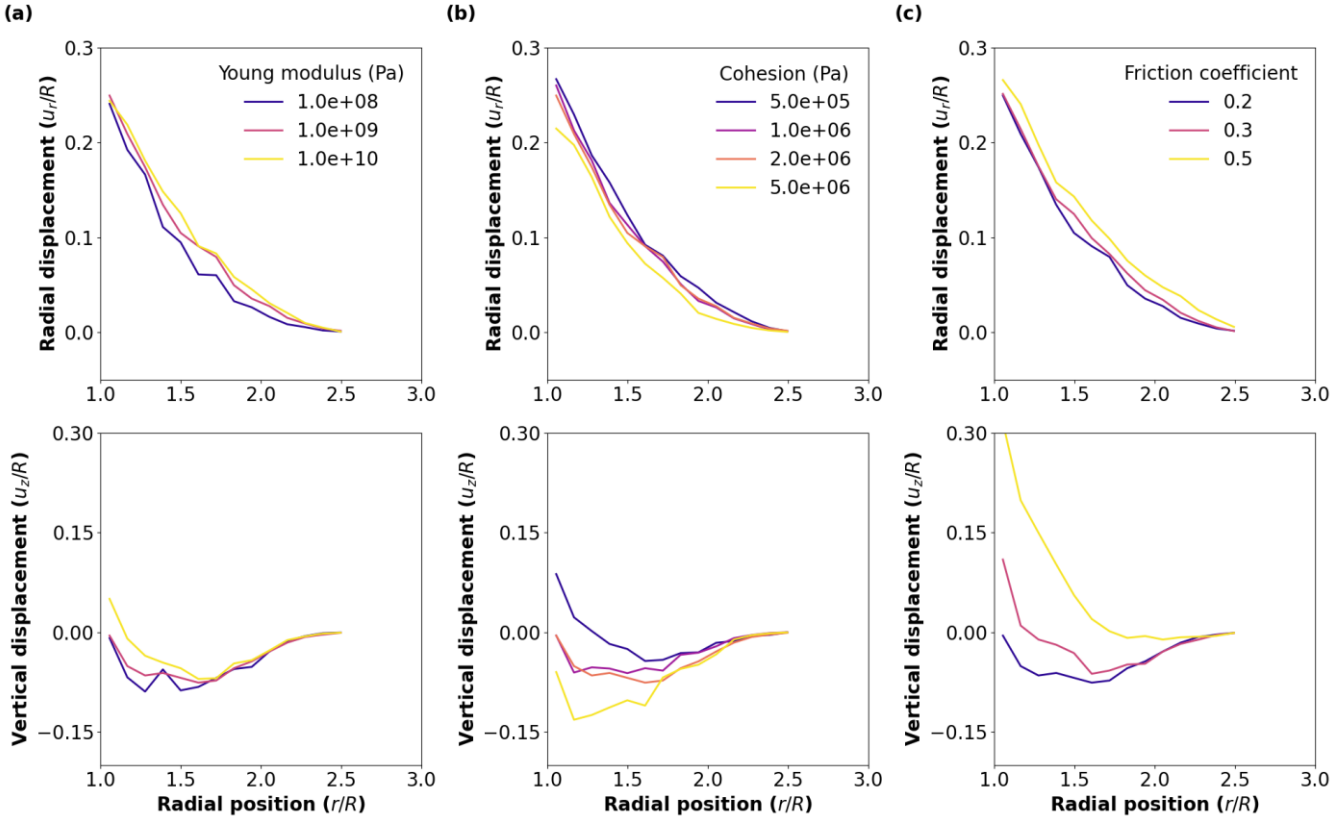

Figure S17: Influence of mechanical parameters on the radial (top) and vertical (bottom) displacement profile obtained with DEM numerical simulations of CPT. The sensitivity analysis has been performed on (a) Young's modulus *E* (Pa) (*C* = 2.0 x 10^6 Pa and

tan(φ) = 0.2), (b) the Cohesion *C* (Pa) (*E* = 1.0 x 10^9 Pa and *tan(φ)* = 0.2) and (c) the Friction coefficient *tan(φ)* (*E* = 1.0 x 10^9 Pa and *C* = 2.0 x 10^6 Pa).

S2.2.3 DH sample

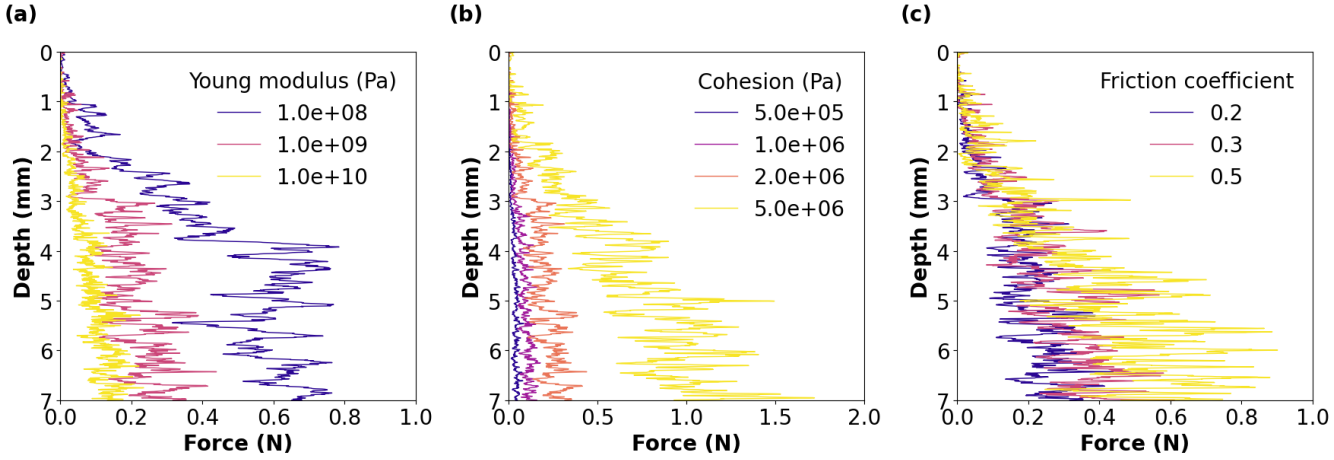

Figure S18: Influence of mechanical parameters on the force profile obtained with DEM numerical simulations of CPT. The sensitivity analysis has been performed on (a) Young's modulus *E* (Pa) (*C* = 2.0 x 10^6 Pa and *tan(φ)* = 0.2), (b) the Cohesion *C* (Pa) (*E* = 1.0 x 10^9 Pa and *tan(φ)* = 0.2) and (c) the Friction coefficient *tan(φ)* (*E* = 1.0 x 10^9 Pa and *C* = 2.0 x 10^6 Pa).

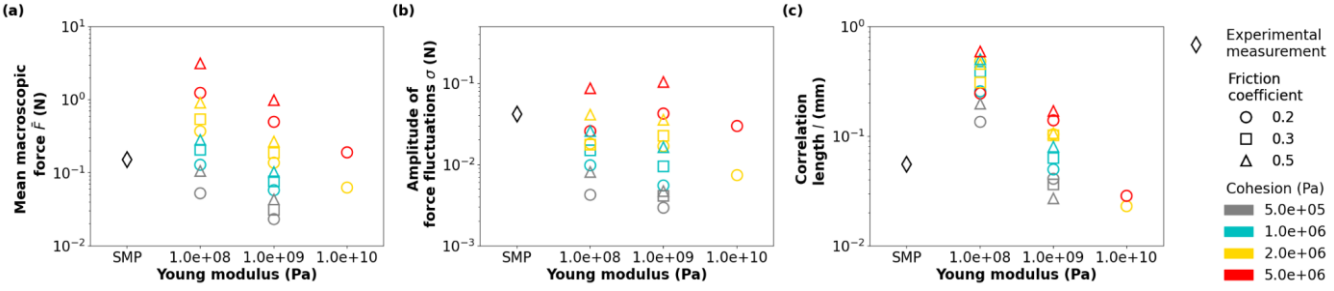

Figure S19: Evolution of statistical indicators as a function of Young's modulus, cohesion and friction angle: (a) Mean macroscopic force $\bar{F}$, (b) amplitude of force fluctuations σ, and (c) correlation length *l*. experimental results (black diamonds) have been added to the plots. The results presented here correspond to the DH sample.

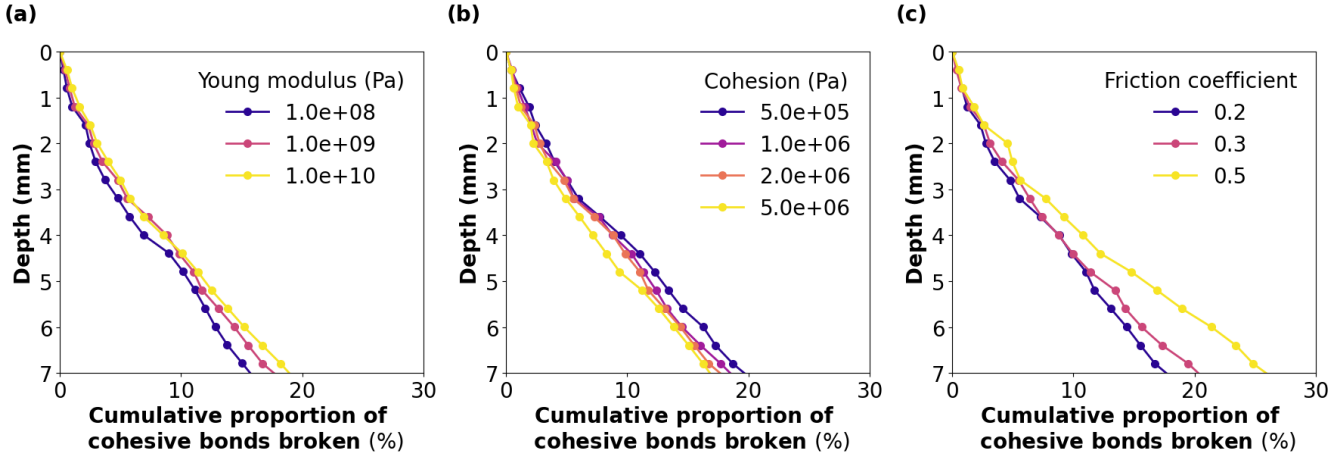

Figure S20: Influence of mechanical parameters on the cumulative number of cohesive bonds as a function of tip penetration depth obtained with DEM numerical simulations of CPT. The sensitivity analysis has been performed on (a) Young's modulus *E* (Pa) (*C* = 2.0 x 10^6 Pa and *tan(φ)* = 0.2), (b) the Cohesion *C* (Pa) (*E* = 1.0 x 10^9 Pa and *tan(φ)* = 0.2) and (c) the Friction coefficient *tan(φ)* (*E* = 1.0 x 10^9 Pa and *C* = 2.0 x 10^6 Pa).

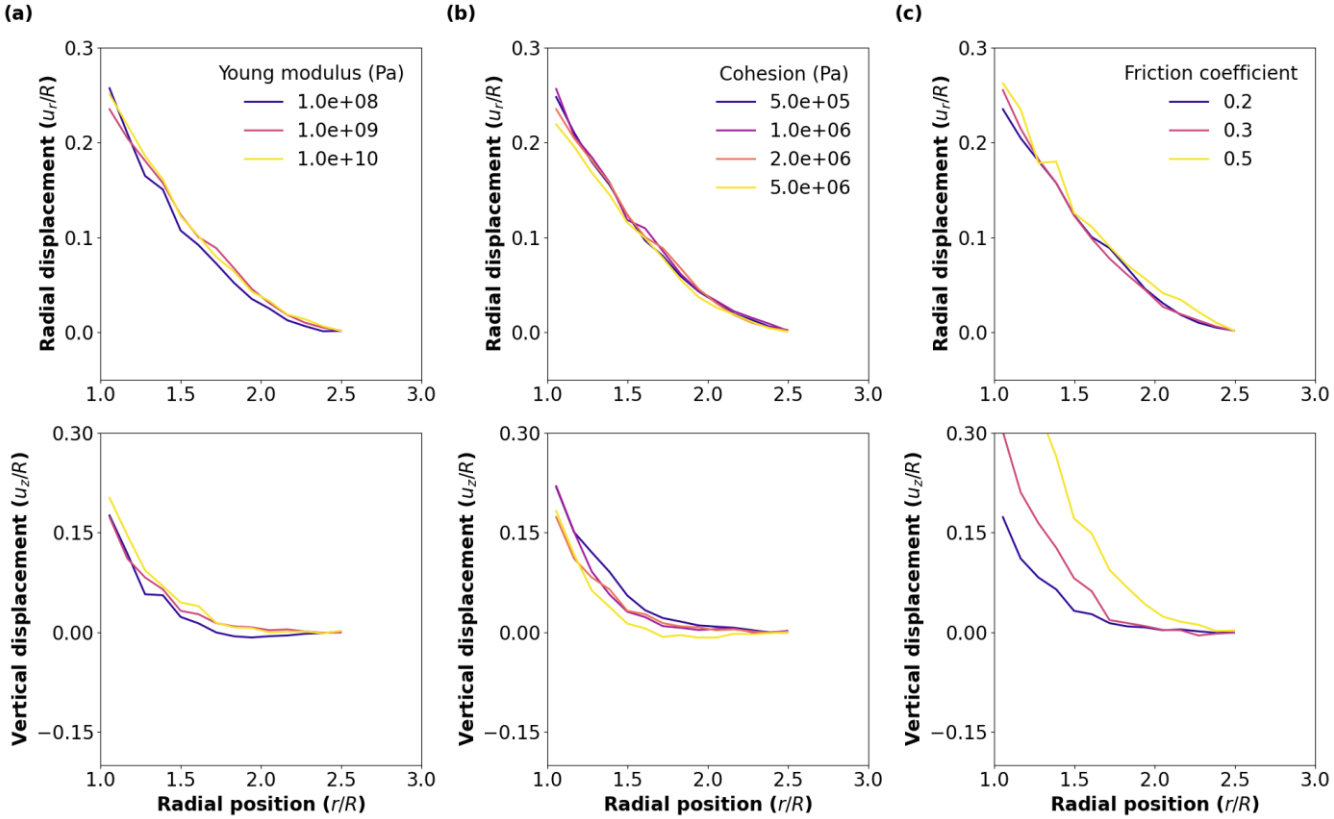

Figure S21: Influence of mechanical parameters on the radial (top) and vertical (bottom) displacement profile obtained with DEM numerical simulations of CPT. The sensitivity analysis has been performed on (a) Young's modulus *E* (Pa) (*C* = 2.0 x 10^6 Pa and

tan(φ) = 0.2), (b) the Cohesion *C* (Pa) (*E* = 1.0 x 10^9 Pa and *tan(φ)* = 0.2) and (c) the Friction coefficient *tan(φ)* (*E* = 1.0 x 10^9 Pa and *C* = 2.0 x 10^6 Pa).

S2.2.4 PP sample

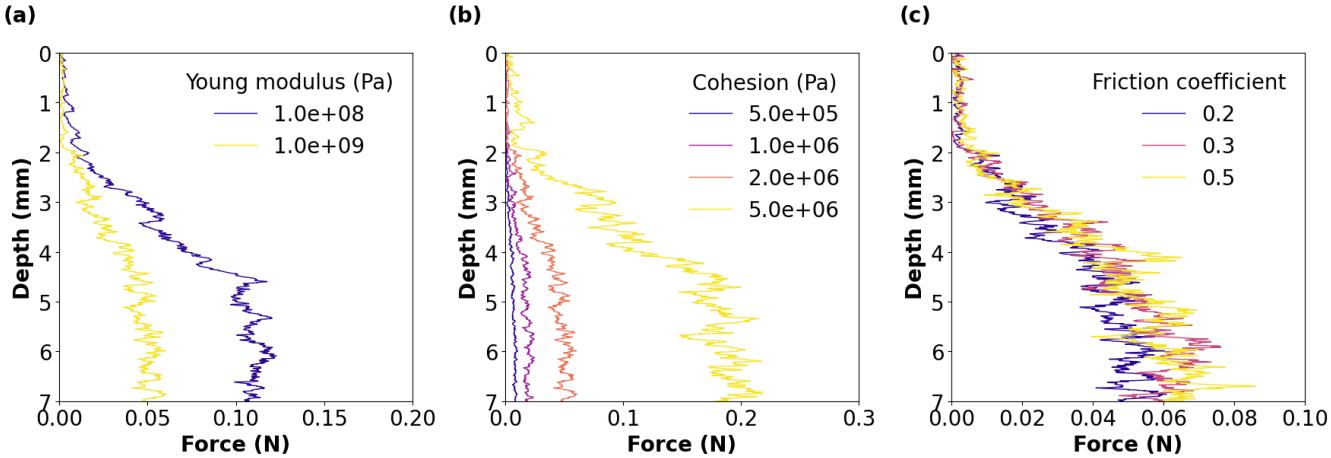

Figure S22: Influence of mechanical parameters on the force profile obtained with DEM numerical simulations of CPT. The sensitivity analysis has been performed on (a) Young's modulus *E* (Pa) (*C* = 1.0 x 10^6 Pa and *tan(φ)* = 0.2), (b) the Cohesion *C* (Pa) (*E* = 1.0 x 10^8 Pa and *tan(φ)* = 0.2) and (c) the Friction coefficient *tan(φ)* (*E* = 1.0 x 10^8 Pa and *C* = 1.0 x 10^6 Pa).

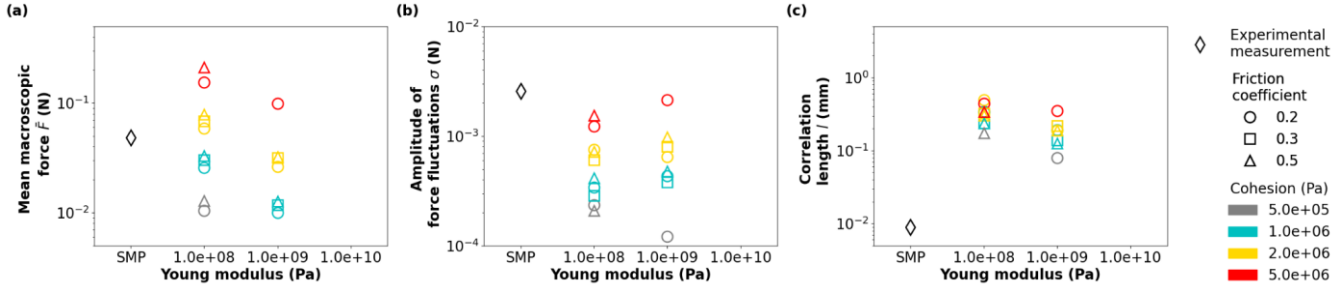

Figure S23: Evolution of statistical indicators as a function of Young's modulus, cohesion and friction coefficient: (a) Mean macroscopic force $\bar{F}$, (b) amplitude of force fluctuations σ, and (c) correlation length *l*. The experimental results (black diamonds) have been added to the plots. The results presented here correspond to the PP sample.

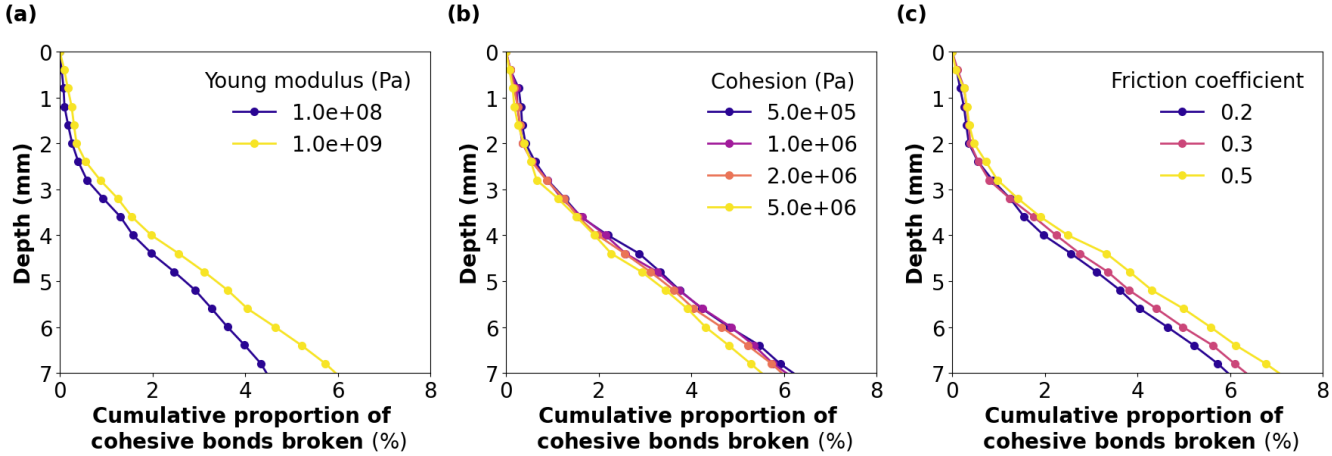

Figure S24: Influence of mechanical parameters on the cumulative number of cohesive bonds as a function of tip penetration depth obtained with DEM numerical simulations of CPT. The sensitivity analysis has been performed on (a) Young's modulus *E* (Pa) (*C* = 2.0 x 10^6 Pa and *tan(φ)* = 0.2), (b) the Cohesion *C* (Pa) (*E* = 1.0 x 10^9 Pa and *tan(φ)* = 0.2) and (c) the Friction coefficient *tan(φ)* (*E* = 1.0 x 10^9 Pa and *C* = 2.0 x 10^6 Pa).

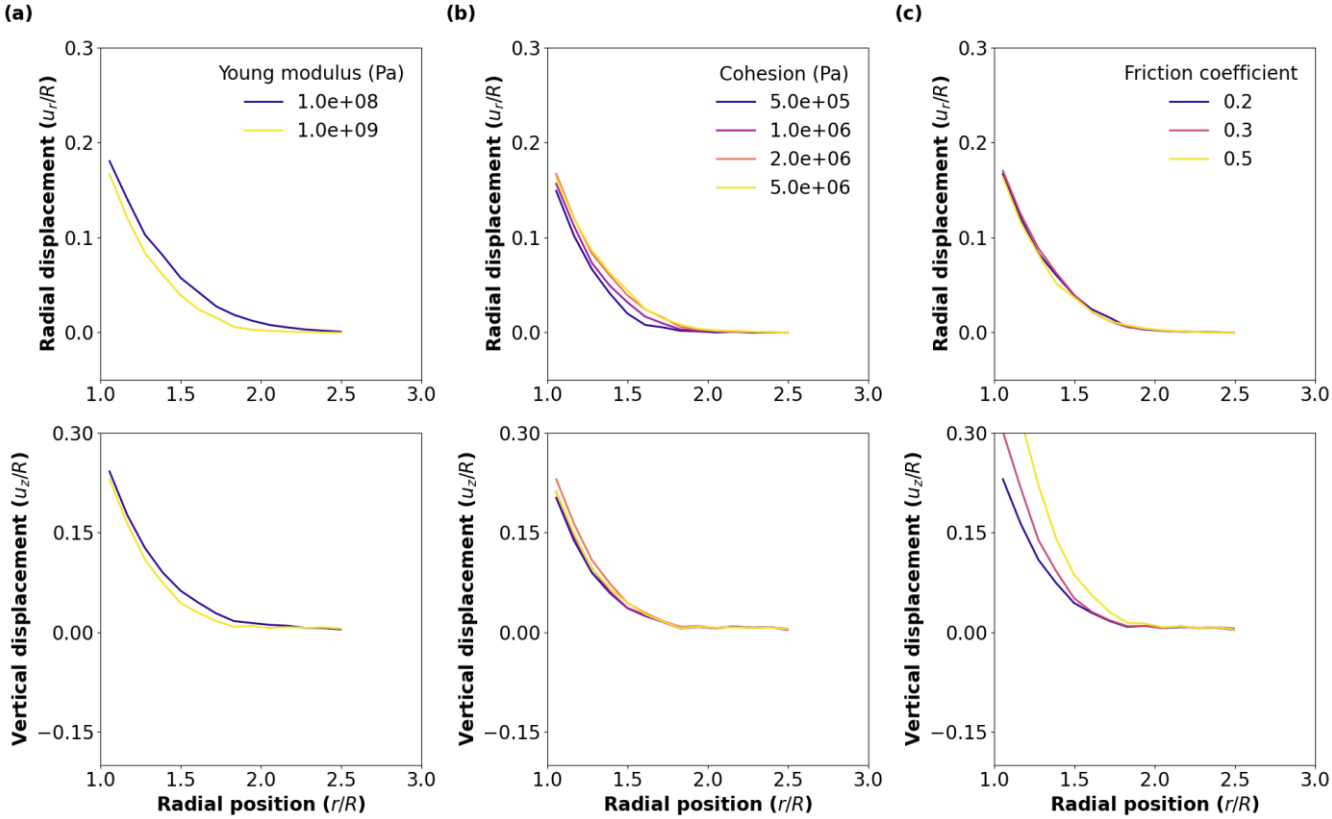

Figure S25: Influence of mechanical parameters on the vertical (top) and radial (bottom) displacement profile obtained with DEM numerical simulations of CPT. The sensitivity analysis has been performed on (a) Young's modulus *E* (Pa) (*C* = 2.0 x 10^6 Pa and

***tan(φ)* = 0.2), (b) the Cohesion *C* (Pa) (*E* = 1.0 x 10^9 Pa and *tan(φ)* = 0.2) and (c) the Friction angle *tan(φ)* (*E* = 1.0 x 10^9 Pa and *C* = 2.0 x 10^6 Pa).**

S2.3 Comparison of DEM model with experimental measurements

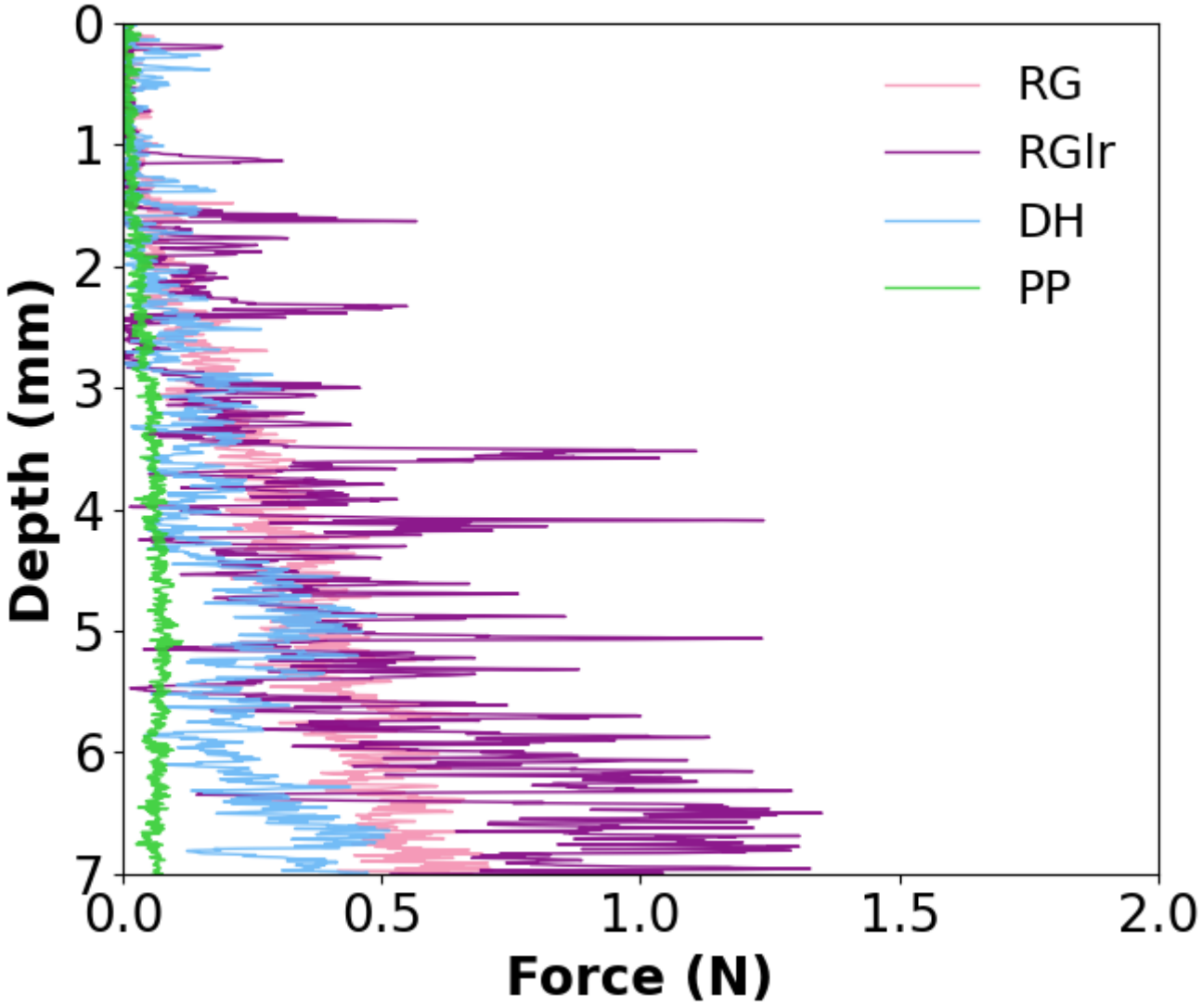

Figure S26: Experimental force profiles obtained with SMP measurements on snow samples.

Sample	$\overline{F}$ (N)	σ (N)	l (mm)
RG	2.5 x 10^{-1}	1.0 x 10^{-2}	1.8 x 10^{-2}

RGlr	3.3×10^{-1}	1.2×10^{-1}	6.3×10^{-2}
DH	1.5×10^{-1}	4.2×10^{-2}	5.6×10^{-2}
PP	4.8×10^{-2}	2.6×-10^{-3}	9.0×10^{-3}

277 **Table S2: Statistical indicators (mean macroscopic force $\overline{F}$, amplitude of force fluctuations σ, correlation length l) obtained for the**
278 **experimental measurements**.
279
280

	E (Pa)	**C (Pa)**	**tan(φ)**	**RE_F**	**RE_σ**	**RE_l**	**RE_{tot}**
RG	1×10^{8}	5×10^{5}	0.2	-1.4×10^{-1}	-4.4×10^{-1}	4.9×10^{-1}	2.1×10^{0}
	1×10^{8}	5×10^{5}	0.3	-1.3×10^{0}	-3.8×10^{-1}	5.2×10^{-1}	1.9×10^{0}
	1×10^{8}	5×10^{5}	0.5	-1.2×10^{-1}	-3.0×10^{-1}	5.0×10^{-1}	1.9×10^{0}
	1×10^{8}	1×10^{6}	0.2	-7.1×10^{-1}	-3.0×10^{-1}	6.1×10^{-1}	1.2×10^{0}
	1×10^{8}	1×10^{6}	0.3	-5.8×10^{-1}	-2.2×10^{-1}	5.7×10^{-1}	1.0×10^{0}
	1×10^{8}	1×10^{6}	0.5	-4.6×10^{-1}	-1.6×10^{-1}	5.9×10^{-1}	8.9×10^{-1}
	1×10^{8}	2×10^{6}	0.2	6.9×10^{-3}	-1.1×10^{-1}	7.2×10^{-1}	7.3×10^{-1}
	1×10^{8}	2×10^{6}	0.3	1.6×10^{-1}	-5.9×10^{-1}	7.7×10^{-1}	8.0×10^{-1}
	1×10^{8}	2×10^{6}	0.5	2.5×10^{-1}	4.2×10^{-2}	7.5×10^{-1}	8.3×10^{-1}
	1×10^{8}	5×10^{6}	0.2	8.4×10^{-1}	3.9×10^{-2}	7.6×10^{1}	1.4×10^{0}
	1×10^{8}	5×10^{6}	0.3	9.9×10^{-1}	1.2×10^{-1}	7.7×10^{1}	1.6×10^{0}
	1×10^{8}	5×10^{6}	0.5	1.1×10^{0}	1.8×10^{-1}	8.2×10^{-1}	1.8×10^{0}
	1×10^{9}	5×10^{5}	0.2	-2.2×10^{0}	-4.9×10^{-1}	1.6×10^{-1}	3.1×10^{0}
	1×10^{9}	5×10^{5}	0.3	-2.0×10^{0}	-4.4×10^{-1}	2.0×10^{-1}	2.9×10^{0}
	1×10^{9}	5×10^{5}	0.5	-1.9×10^{0}	-3.9×10^{-1}	1.7×10^{-1}	2.7×10^{0}
	1×10^{9}	1×10^{6}	0.2	-1.5×10^{0}	-2.8×10^{-1}	3.4×10^{-1}	2.1×10^{0}
	1×10^{9}	1×10^{6}	0.3	-1.5×10^{0}	-2.5×10^{-1}	2.8×10^{-1}	2.1×10^{0}
	1×10^{9}	1×10^{6}	0.5	-1.3×10^{0}	-1.5×10^{-1}	3.6×10^{-1}	1.9×10^{0}
	1×10^{9}	2×10^{6}	0.2	-8.8×10^{-1}	-9.0×10^{-2}	4.2×10^{-1}	1.3×10^{0}
	1×10^{9}	2×10^{6}	0.3	-6.9×10^{-1}	2.8×10^{-2}	5.5×10^{-1}	1.1×10^{0}
	1×10^{9}	2×10^{6}	0.5	-6.4×10^{-1}	-2.9×10^{-2}	3.7×10^{-1}	9.9×10^{-1}
	1×10^{9}	5×10^{6}	0.2	1.2×10^{-1}	1.2×10^{-1}	5.2×10^{-1}	5.6×10^{-1}
	1×10^{9}	5×10^{6}	0.3	2.7×10^{-1}	1.6×10^{-1}	5.0×10^{-1}	6.5×10^{-1}
	1×10^{9}	5×10^{6}	0.5	3.6×10^{-1}	2.1×10^{-1}	5.2×10^{-1}	7.6×10^{-1}
	1×10^{10}	5×10^{5}	0.2	-3.0×10^{0}	-7.1×10^{-1}	-2.6×10^{-2}	4.3×10^{0}
	1×10^{10}	1×10^{6}	0.2	-2.2×10^{0}	-4.4×10^{-1}	6.7×10^{-3}	3.1×10^{0}
	1×10^{10}	2×10^{6}	0.2	-1.5×10^{0}	-1.6×10^{-1}	1.4×10^{-1}	2.2×10^{0}
	1×10^{10}	2×10^{6}	0.5	-1.3×10^{0}	-1.5×10^{-1}	3.7×10^{-2}	1.8×10^{0}
	1×10^{10}	5×10^{6}	0.2	-6.9×10^{-1}	1.3×10^{-1}	2.4×10^{-1}	1.0×10^{0}
	1×10^{10}	5×10^{6}	0.5	-4.6×10^{-1}	2.2×10^{-1}	2.3×10^{-1}	7.2×10^{-1}
RGlr	1×10^{8}	5×10^{5}	0.2	-5.1×10^{-1}	-9.6×10^{-1}	5.1×10^{-1}	1.3×10^{0}
	1×10^{8}	5×10^{5}	0.3	-4.5×10^{-2}	-8.3×10^{-1}	6.3×10^{-1}	1.0×10^{0}
	1×10^{8}	5×10^{5}	0.5	5.3×10^{-1}	-5.2×10^{-1}	8.0×10^{-1}	1.2×10^{0}
	1×10^{8}	1×10^{6}	0.2	3.1×10^{-1}	-7.6×10^{-1}	6.5×10^{-1}	1.1×10^{0}
	1×10^{8}	1×10^{6}	0.3	8.8×10^{-1}	-4.8×10^{-1}	5.2×10^{-1}	1.4×10^{0}

	1×10^{8}	1×10^{6}	0.5	1.5×10^{0}	-4.1×10^{-2}	1.1×10^{0}	2.4×10^{0}
	1×10^{8}	2×10^{6}	0.2	1.2×10^{0}	-3.9×10^{-1}	7.3×10^{-1}	1.9×10^{0}
	1×10^{8}	2×10^{6}	0.3	1.7×10^{0}	-9.6×10^{-2}	8.9×10^{-1}	2.6×10^{0}
	1×10^{8}	2×10^{6}	0.5	2.5×10^{0}	3.7×10^{-1}	8.4×10^{-1}	3.6×10^{0}
	1×10^{8}	5×10^{6}	0.2	2.3×10^{0}	-8.1×10^{-2}	6.9×10^{-1}	3.3×10^{0}
	1×10^{8}	5×10^{6}	0.3	2.8×10^{0}	1.6×10^{-1}	6.9×10^{-1}	4.0×10^{0}
	1×10^{8}	5×10^{6}	0.5	3.5×10^{0}	3.8×10^{-1}	9.1×10^{-1}	5.0×10^{0}
	1×10^{9}	5×10^{5}	0.2	-1.2×10^{0}	-1.0×10^{0}	-8.9×10^{-2}	2.0×10^{0}
	1×10^{9}	5×10^{5}	0.3	-8.2×10^{-1}	-8.8×10^{-1}	-5.6×10^{-2}	1.5×10^{0}
	1×10^{9}	5×10^{5}	0.5	-4.1×10^{-1}	-4.2×10^{-1}	1.3×10^{-1}	7.3×10^{-1}
	1×10^{9}	1×10^{6}	0.2	-4.7×10^{-1}	-7.2×10^{-1}	1.9×10^{-3}	9.8×10^{-1}
	1×10^{9}	1×10^{6}	0.3	5.5×10^{-2}	-4.6×10^{-1}	1.1×10^{-1}	4.8×10^{-1}
	1×10^{9}	1×10^{6}	0.5	3.6×10^{-1}	-1.2×10^{-1}	2.2×10^{-1}	5.6×10^{-1}
	1×10^{9}	2×10^{6}	0.2	3.9×10^{-1}	-2.8×10^{-1}	1.5×10^{-1}	6.3×10^{-1}
	1×10^{9}	2×10^{6}	0.3	7.6×10^{-1}	-8.2×10^{-2}	2.3×10^{-1}	1.1×10^{0}
	1×10^{9}	2×10^{6}	0.5	1.2×10^{0}	4.4×10^{-1}	3.1×10^{-1}	1.7×10^{0}
	1×10^{9}	5×10^{6}	0.2	1.4×10^{0}	1.5×10^{-1}	2.7×10^{-1}	2.0×10^{0}
	1×10^{9}	5×10^{6}	0.3	1.9×10^{0}	2.8×10^{-1}	3.8×10^{-1}	2.8×10^{0}
	1×10^{9}	5×10^{6}	0.5	2.4×10^{0}	9.3×10^{-1}	7.6×10^{-1}	3.7×10^{0}
	1×10^{10}	5×10^{5}	0.2	-2.2×10^{0}	-1.9×10^{0}	-3.6×10^{-1}	3.6×10^{0}
	1×10^{10}	5×10^{5}	0.3	-1.6×10^{0}	-1.4×10^{0}	-2.8×10^{-1}	2.7×10^{0}
	1×10^{10}	5×10^{5}	0.5	-1.1×10^{0}	-9.9×10^{-1}	-4.6×10^{-1}	1.9×10^{0}
	1×10^{10}	1×10^{6}	0.2	-1.1×10^{0}	-1.0×10^{0}	-3.6×10^{-1}	1.9×10^{0}
	1×10^{10}	1×10^{6}	0.3	-7.1×10^{-1}	-8.4×10^{-1}	-4.1×10^{-1}	1.4×10^{0}
	1×10^{10}	1×10^{6}	0.5	-2.6×10^{-1}	-5.1×10^{-1}	-4.8×10^{-1}	7.9×10^{-1}
	1×10^{10}	2×10^{6}	0.2	-2.6×10^{-1}	-4.2×10^{-1}	-4.0×10^{-1}	6.9×10^{-1}
	1×10^{10}	2×10^{6}	0.3	1.5×10^{-1}	-2.5×10^{-1}	-4.5×10^{-1}	5.6×10^{-1}
	1×10^{10}	2×10^{6}	0.5	5.3×10^{-1}	1.8×10^{-1}	-3.8×10^{-1}	8.6×10^{-1}
	1×10^{10}	5×10^{6}	0.2	7.3×10^{-1}	1.2×10^{-1}	-3.4×10^{-1}	1.1×10^{0}
	1×10^{10}	5×10^{6}	0.3	1.1×10^{0}	3.8×10^{-1}	-2.5×10^{-1}	1.6×10^{0}
	1×10^{10}	5×10^{6}	0.5	1.4×10^{0}	6.8×10^{-1}	-2.5×10^{-1}	2.1×10^{0}
DH	1×10^{8}	5×10^{5}	0.2	-5.6×10^{-1}	-7.2×10^{-1}	3.1×10^{-1}	1.1×10^{0}
	1×10^{8}	5×10^{5}	0.5	-1.9×10^{-1}	-5.2×10^{-1}	4.4×10^{-1}	7.3×10^{-1}
	1×10^{8}	1×10^{6}	0.2	-8.6×10^{-2}	-4.6×10^{-1}	5.3×10^{-1}	7.1×10^{-1}
	1×10^{8}	1×10^{6}	0.3	1.6×10^{-1}	-3.2×10^{-1}	6.7×10^{-1}	7.8×10^{-1}
	1×10^{8}	1×10^{6}	0.5	3.3×10^{-1}	-1.5×10^{-1}	7.6×10^{-1}	9.1×10^{-1}
	1×10^{8}	2×10^{6}	0.2	4.7×10^{-1}	-2.6×10^{-1}	7.5×10^{-1}	1.0×10^{0}
	1×10^{8}	2×10^{6}	0.3	6.7×10^{-1}	-2.7×10^{-1}	5.9×10^{-1}	1.2×10^{0}
	1×10^{8}	2×10^{6}	0.5	9.5×10^{-1}	-6.4×10^{-3}	7.3×10^{-1}	1.5×10^{0}
	1×10^{8}	5×10^{6}	0.2	1.1×10^{0}	-1.5×10^{-1}	5.1×10^{-1}	1.7×10^{0}
	1×10^{8}	5×10^{6}	0.5	1.6×10^{0}	2.3×10^{-1}	8.2×10^{-1}	2.4×10^{0}
	1×10^{9}	5×10^{5}	0.2	-9.9×10^{-1}	-8.4×10^{-1}	-1.1×10^{-1}	1.6×10^{0}
	1×10^{9}	5×10^{5}	0.3	-8.4×10^{-1}	-7.3×10^{-1}	-1.5×10^{-1}	1.4×10^{0}
	1×10^{9}	5×10^{5}	0.5	-6.6×10^{-1}	-6.9×10^{-1}	-2.5×10^{-1}	1.2×10^{0}
	1×10^{9}	1×10^{6}	0.2	-5.1×10^{-1}	-6.4×10^{-1}	-4.1×10^{-2}	9.6×10^{-1}
	1×10^{9}	1×10^{6}	0.3	-3.6×10^{-1}	-4.7×10^{-1}	4.5×10^{-2}	7.0×10^{-1}

	1×10^{9}	1×10^{6}	0.5	-2.0×10^{-1}	-3.0×10^{-1}	1.3×10^{-1}	4.3×10^{-1}
	1×10^{9}	2×10^{6}	0.2	-5.4×10^{-2}	-2.9×10^{-1}	2.2×10^{-1}	3.7×10^{-1}
	1×10^{9}	2×10^{6}	0.3	1.1×10^{-1}	-2.0×10^{-1}	2.1×10^{-1}	3.3×10^{-1}
	1×10^{9}	2×10^{6}	0.5	3.0×10^{-1}	-5.2×10^{-2}	2.3×10^{-1}	4.8×10^{-1}
	1×10^{9}	5×10^{6}	0.2	6.3×10^{-1}	5.1×10^{-3}	3.1×10^{-1}	9.5×10^{-1}
	1×10^{9}	5×10^{6}	0.5	9.9×10^{-1}	2.9×10^{-1}	3.9×10^{-1}	1.5×10^{0}
	1×10^{10}	2×10^{6}	0.2	-4.6×10^{-1}	-5.5×10^{-1}	-3.1×10^{-1}	9.1×10^{-1}
	1×10^{10}	5×10^{6}	0.2	1.2×10^{-1}	-1.1×10^{-1}	-2.3×10^{-1}	3.1×10^{-1}
PP	1×10^{8}	5×10^{5}	0.2	-5.1×10^{-1}	-4.0×10^{-1}	7.7×10^{-1}	1.1×10^{0}
	1×10^{8}	5×10^{5}	0.5	-4.4×10^{-1}	-4.2×10^{-2}	6.3×10^{-1}	9.8×10^{-1}
	1×10^{8}	1×10^{6}	0.2	-2.1×10^{-1}	-3.4×10^{-1}	7.7×10^{-1}	8.9×10^{-1}
	1×10^{8}	1×10^{6}	0.3	-1.5×10^{-1}	-3.7×10^{-1}	7.0×10^{-1}	8.2×10^{-1}
	1×10^{8}	1×10^{6}	0.5	-1.2×10^{-1}	-3.1×10^{-1}	6.9×10^{-1}	7.8×10^{-1}
	1×10^{8}	2×10^{6}	0.2	6.5×10^{-2}	-2.1×10^{-1}	8.5×10^{0}	8.8×10^{-1}
	1×10^{8}	2×10^{6}	0.3	1.2×10^{-1}	-2.4×10^{-1}	7.6×10^{-1}	8.1×10^{-1}
	1×10^{8}	2×10^{6}	0.5	1.6×10^{-1}	-2.1×10^{-1}	7.5×10^{-1}	8.1×10^{-1}
	1×10^{8}	5×10^{6}	0.2	3.9×10^{-1}	-1.2×10^{-1}	8.3×10^{-1}	1.0×10^{0}
	1×10^{8}	5×10^{6}	0.5	4.9×10^{-1}	-8.5×10^{-2}	7.7×10^{-1}	1.0×10^{0}
	1×10^{9}	5×10^{5}	0.2	-8.2×10^{-1}	-5.1×10^{-1}	4.6×10^{-1}	1.3×10^{0}
	1×10^{9}	1×10^{6}	0.2	-5.2×10^{-1}	-3.0×10^{-1}	6.5×10^{-1}	1.0×10^{0}
	1×10^{9}	1×10^{6}	0.3	-4.6×10^{-1}	-3.2×10^{-1}	5.8×10^{-1}	9.3×10^{-1}
	1×10^{9}	1×10^{6}	0.5	-4.4×10^{-1}	-2.8×10^{-1}	5.6×10^{-1}	8.8×10^{-1}
	1×10^{9}	2×10^{6}	0.2	-2.0×10^{-1}	-2.3×10^{-1}	6.5×10^{-1}	7.4×10^{-1}
	1×10^{9}	2×10^{6}	0.3	-1.4×10^{-1}	-2.0×10^{-1}	6.8×10^{-1}	7.3×10^{-1}
	1×10^{9}	2×10^{6}	0.5	-1.3×10^{-1}	-1.6×10^{-1}	6.5×10^{-1}	6.9×10^{-1}
	1×10^{9}	5×10^{6}	0.2	2.4×10^{-1}	-3.0×10^{-2}	7.8×10^{-1}	8.5×10^{-1}

Table S3: Combinations of all the mechanical parameters (Young's modulus *E*, cohesion *C* and friction coefficient *tan(φ)*) tested for RG, RGlr, DH and PP samples. The errors on the statistical indicators (mean force $\overline{F}$, amplitude of force fluctuations σ, correlation length *l*) were computed as the logarithmic relative error RE_k (Eq. 9) compared to the experimental values (Table S2). Negative error value indicates an underestimation and positive error value indicates an overestimation. The total error RE_{tot} is calculated with (Eq. 8) and the minimal value is used to select the best set of mechanical parameters for each sample.

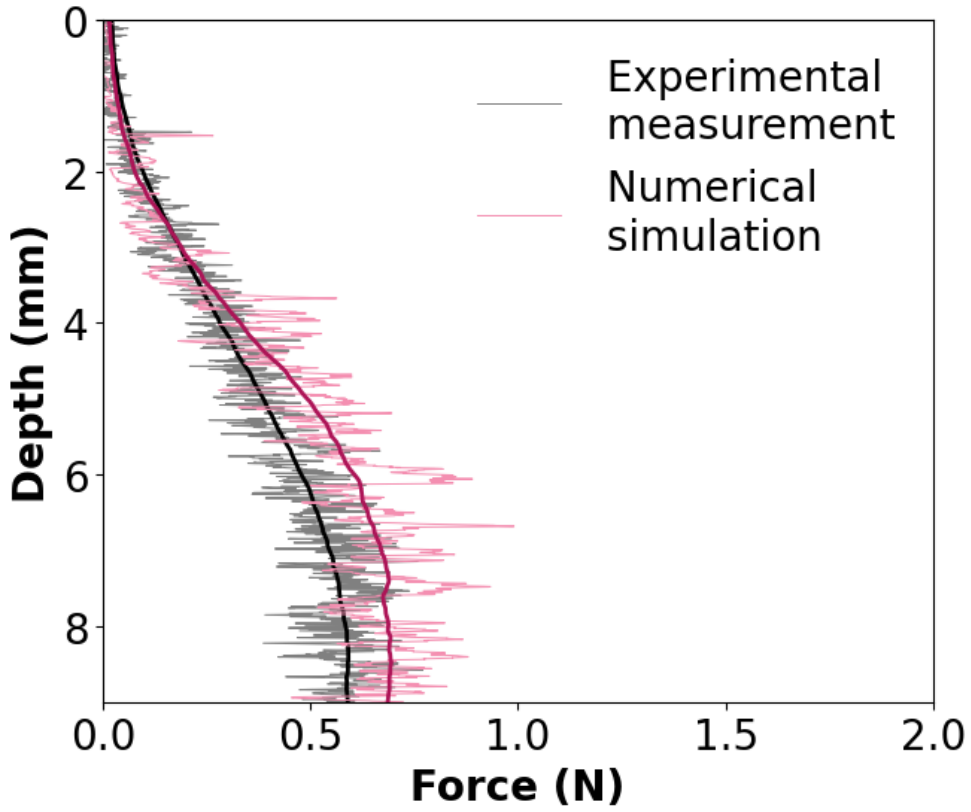

Figure S27: Experimental (grey) and numerical (coloured) force profiles obtained by CPT for RG sample. The numerical profiles correspond to the best fit of mechanical parameters (Table 3). The superposed smoothed profile (bold line) corresponds to the average force value over a rolling window of 3 mm.

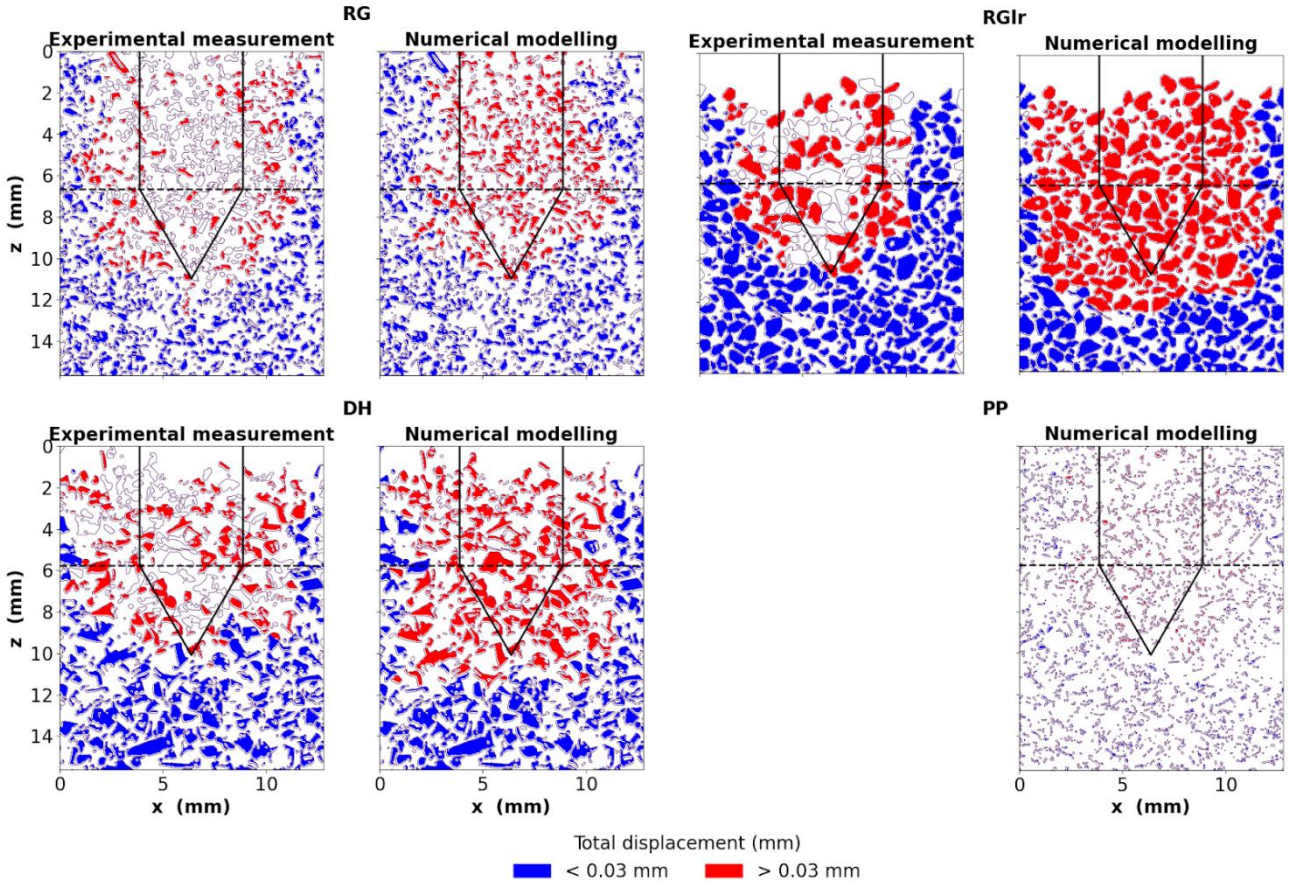

Figure S28: Total displacement maps obtained experimentally with µCT (left) and numerically with DEM simulation (right) for RG, RGlr, DH and PP samples. A displacement threshold of 0.03 mm has been set to define the deformation zone (Peinke et al. 2020). No coloured filled grains correspond to non-trackable grains in µCT scans (Peinke et al. 2020) and deleted grains in the DEM grain shape representation. The tip position is indicated with black solid lines. The horizontal black dashed line indicates the cone top. The displacement profiles are computed from the sample surface to the cone top. Results are obtained with the mechanical parameters E = 1 x 10^9 Pa, C = 2 x 10^6 Pa and $tan(\varphi)$ = 0.2 (Table S3).

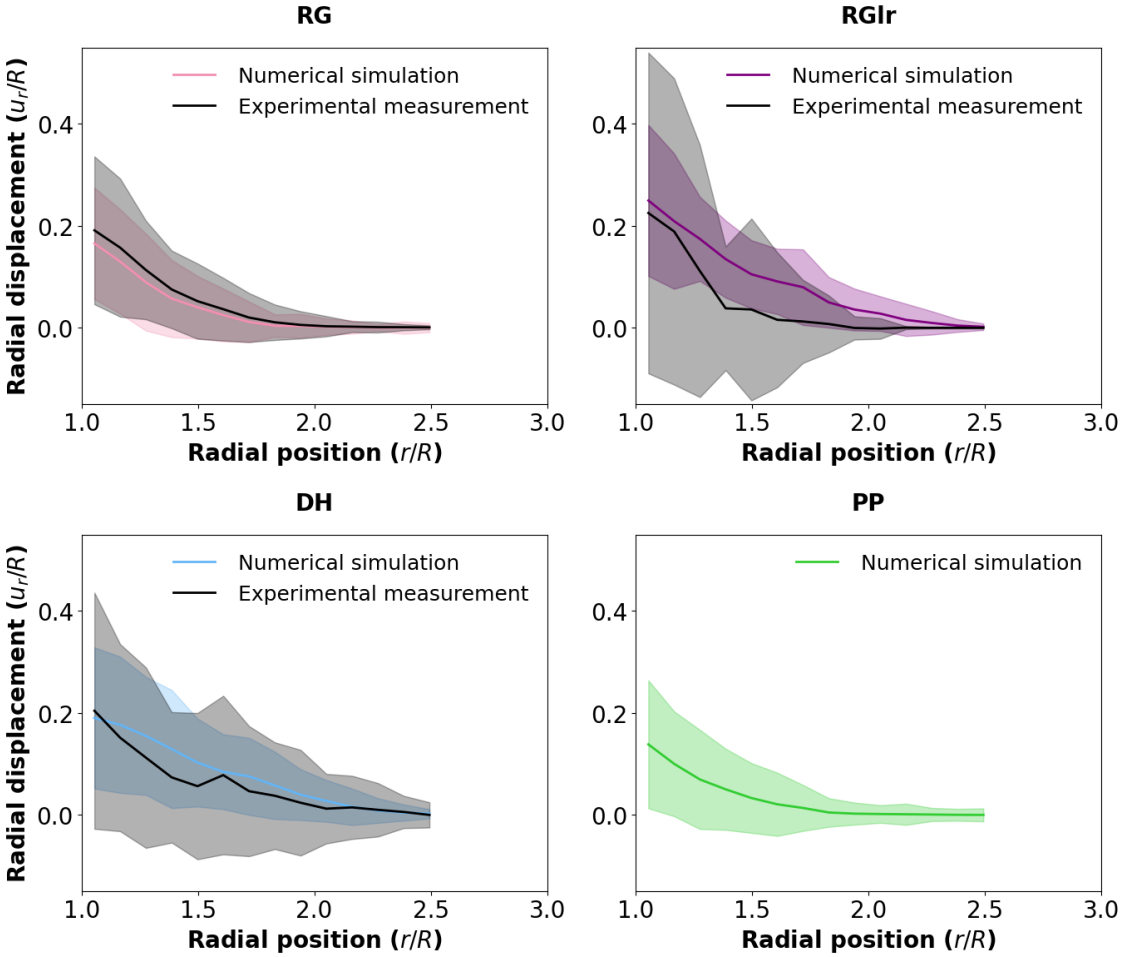

Figure S29: Radial displacement profiles (solid lines) obtained experimentally (black) and numerically (coloured) for the RG, RGlr, DH and PP samples. The shadowed areas around the solid lines correspond to the standard deviation of grain displacement translating the variability of the radial displacement of grains. Results are obtained with the mechanical parameters E = 1 x 10^9 Pa, C = 2 x 10^6 Pa and $tan(\varphi)$ = 0.2 (Table S3).

S3 Scaling law of the mean force

Sample	α	β	$\bar{\lambda}$ (mm^{-1})
RG	-0.48	1.37	1.43
RGlr	-0.43	1.29	4.88
DH	-0.43	1.35	2.99

PP	-0.36	1.27	0.87

Table S4: Exponents α *and* β are power law exponents obtained from the mean macroscopic force $\overline{F}$ value dependence on the Young's modulus *E* and cohesion *C* respectively (Figs. 5 (a), S15 (a), S19 (a), S23 (a)). Exponents of each snow type are averaged values of exponents computed for fixed values of the mechanical parameters not involved in the power law. $\bar{\lambda}$ corresponds to the slope of the proportion of cohesive bonds broken by depth unit (mm^{-1}) (Figs. 2 (b), S6 (b), S8 (b), S10 (b)). The slope values obtained for the mechanical parameters *E* and *C* presented in Table S3 are averaged. All the results are provided for a friction coefficient *tan(φ)* of 0.3.